ORIGINAL PAPER

Experimental Study on Pore Variation and Meso-Damage of Saturated Sandstone Under Unloading Condition

Jianxin Fu[1,2] · Wenchao Chen[1,2] · Yuye Tan[1,2] · Jie Wang[1,2] · Weidong Song[1,2]

Abstract

To study the fracture propagation and meso damage evolution law of saturated sandstone under unloading (unloading confining pressure), three unloading confining pressure tests of sandstone under different initial axial pressures were designed. By means of nuclear magnetic resonance (NMR) technology, the variation characteristics of rock porosity and T_2 spectrum curves were analyzed, the relationship between damage degree and unloading confining pressure ratio was established, and the fractal characteristics of NMR were analyzed. The results show that: (1) The larger the initial axial compression, the larger the axial strain and the smaller the radial strain when unloading failure occurs. With the increase of unloading confining pressure ratio, the elastic modulus decreases, and the Poisson's ratio and strain increase. (2) T_2 spectrum peak shows that the pore size increases with the increase of unloading confining pressure ratio. The larger the initial axial compression, the larger the pore size. (3) Porosity increases exponentially with the increase of unloading confining pressure ratio, in which the number of micropores continues to increase, the number of mesopores and macropores first decreases and then increases. The initial axial pressure promotes the development and expansion of pores. (4) The relationship between pore characteristics, energy and damage degree is generally consistent, and the fractal characteristics of three sizes of pores show different changing rules with the increase of unloading confining pressure ratio.

Highlights

- With the increase of unloading confining pressure ratio, the rock gradually changes from elastic deformation to plastic deformation.
- The failure of the sample is caused by the sharp increase of the number and size of pores.
- Porosity increases exponentially with the increase of unloading confining pressure ratio.
- With the increase of unloading confining pressure ratio, the number of micropores continues to increase, and the number of mesopores and macropores first decreases and then increases.

✉ Wenchao Chen
   1301590435@qq.com

✉ Yuye Tan
   tanyuye@ustb.edu.cn

1   School of Civil and Resources Engineering, University of Science and Technology Beijing, Beijing 100083, China

2   State Key Laboratory of High-Efficient Mining and Safety of Metal Mines of Ministry of Education, University of Science and Technology Beijing, Beijing 100083, China

1 Introduction

Before the excavation of the underground rock mass, the surrounding stress field is in a relatively stable and balanced state. After excavation disturbance, the rock mass stress will be redistributed within a certain range. Rock deformation occurs in the process of stress distribution. Low strength or stress concentration leads to local failure, resulting in the overall instability of the project (Feng and Jiang. 2015; Fu et al. 2017a, b; Li et al. 2014). The essence of the instability of goaf is the overall instability caused by the damage and fracture of surrounding rock under the action of stress. The stress state of rock mass changes, which is manifested as

the unloading effect. When the unloading degree exceeds the bearing limit of rock mass, the unloading failure occurs (Fu et al. 2017a, b; Fu et al. 2018; Huang and Huang. 2014).

In actual mine engineering, many geological disasters are closely related to water (Al-Shalabi and Sepehrnoori. 2016; Zilong et al. 2016). Therefore, the influence of water on the mechanical properties of rock must be considered in the excavation of underground rock mass. Numerous academic studies have shown that the strength and hardness of saturated sandstone are significantly lower than those of dry sandstone (BV 2005). By analyzing the mechanical properties of dry sandstone and water-saturated sandstone under different loading rates, it is concluded that the strength of saturated sandstone is lower than that of dry sandstone, and the difference in rock strength between the two states decreases with the increase of deformation rate (Teng and Peng. 2020). A series of triaxial compression tests of dry sandstone and saturated sandstone have been carried out. And it is found that the cohesion, internal friction angle and elastic modulus of sandstone decrease while Poisson's ratio increases after water saturation. Saturated sandstone is more prone to crack during loading, and the damage is relatively mild. For dry sandstone, rock burst often occurs (Diyuan et al. 2019).

Compared with the conventional mechanical loading mode, the stress state changes of rock mass under the unloading effect are obviously different, and there are obvious differences in the change of rock mass mechanical parameters, rock mass deformation and crack propagation mode (Huang and Li. 2014; Meng et al. 2016; Xue et al. 2021). The strength deterioration of rock mass at the macro scale is manifested as the decrease of cohesion and the increase of internal friction angle (Zhang et al. 2015), and at the mesoscopic scale is manifested as the uneven expansion of internal cracks. The strength deterioration of rock is the essential reason for the instability and failure of the rock mass. In view of such mechanical problems, carry out research on the mechanical characteristics of rock under unloading conditions, analyze the change characteristics of fracture structure in the rock mass, and deeply explore the damage evolution process and failure mechanism of rock mass, which is conducive to accurately reveal the unloading deformation and failure mechanism of surrounding rock in goaf, analyze and predict the stability of goaf.

At present, a series of studies on the mechanical properties of rock unloading have been carried out by many scholars. Based on the occurrence environment of rock mass and the characteristics of excavation disturbance, the deformation and failure characteristics of rock under different stress states were analyzed by means of an indoor test, theoretical research and numerical simulation. Rock mechanics test under confining pressure with different unloading rates and numerical simulation analysis were carried out. They

found that the greater the unloading rate, the more splitting cracks and more complete failure, and the failure mode of rock changes from shear failure to tensile fracture (Huang and Li. 2014; Kang et al. 2020; Li et al. 2019; Zhang et al. 2018). The mechanical tests of rock under different unloading conditions were carried out to study the characteristics of rock deformation and failure. The results show that the non-uniform deformation of rock was concentrated on the side during unloading failure, and the phenomena of deformation, fracture and fragment ejection occurred, which provided a theoretical basis for unstable failure and rock-burst disaster in the unloading process of surrounding rock (Ding et al. 2016; Duan et al. 2019; Zhao et al. 2014). The unloading test of sandstone under different confining pressure was carried out, and the relationship between crack propagation characteristics and confining pressure was analyzed. It indicates that the crack closure stress, crack initiation stress and crack damage stress of sandstone gradually increase with the increase of confining pressure level (Chen et al. 2020). Through the constant axial pressure unloading confining pressure test of sandstone, it was found that the axial deformation, failure confining pressure and shear fracture energy in the process of failure are positively correlated with the initial confining pressure, the amount of dilatancy, dilatancy velocity and radial deformation are negatively correlated with the initial confining pressure, and the damage velocity in the unloading stage is significantly greater than that in the loading stage (Hou et al. 2021).

NMR testing system can quantitatively analyze the number and dimension variation of pores with different sizes in rock, which is widely used in the study of meso internal damage of rock (Alam et al. 2014; Olatinsu et al. 2017; Zhou et al. 2021a, b). To study the unloading characteristics of marble under different stress conditions, NMR technology was used to obtain the parameter characteristics such as porosity and T_2 spectrum distribution of rock samples, so as to carry out the meso study of the change of fracture structure in rock and the influence of initial stress on fracture propagation (Hu et al. 2014; Zhou et al. 2014a, b, 2018a, b). The pore structure was characterized by NMR, and the pores were divided into micro pores, secondary pores and main pores (Zhang et al. 2021a, b). Based on NMR technology and mechanical test of sandstone under different conditions, rock meso damage mechanism, T_2 cut-off characteristic analysis, pore size distribution change, water migration law were deeply studied (Chu et al. 2021; Gao et al. 2017; Li et al. 2020; Lyu et al. 2020; Shen et al. 2020). The porosity and pore size distribution of sandstone in different chemical solutions were measured by NMR technology, and the signal variation law of water in pores with different sizes was obtained by inversion (Lin et al. 2020).

The research on the damage evolution model is mainly based on the theory of continuum mechanics. The damage

variables of rock are introduced from the weakening of some mechanical parameters and internal defects, and the damage evolution model was deduced from the damage variables. The internal instability mechanism was deeply studied through the rock damage evolution model (Barsanescu. 2015; Fu et al. 2020). The mechanical properties of strength deterioration, damage evolution law, overall instability failure mechanism and constitutive model of the sample were analyzed by acoustic emission and other test methods (Wang et al. 2020; Wang et al. 2021a, b, c; Wang et al. 2022a, b). The change laws of energy dissipation and secant modulus during unloading were defined and analyzed, and the key stages of rock damage evolution were effectively distinguished based on the change of damage index (Dai et al. 2018). Rock mechanics tests with different unloading rates were carried out to analyze the deformation and damage evolution process of surrounding rock under the condition of excavation and unloading. The results show that the deformation and damage of surrounding rock after unloading are generated and accumulated in the maintenance stage (Hou et al. 2020a, b). The nonlinear evolution law of deformation and damage of sandstone under conventional triaxial loading and unloading was studied, and the damage evolution equation and constitutive model of sandstone under conventional loading and unloading were established by deriving the energy balance equation (Zhou et al. 2021a, b).

Based on the above research methods and results, there have been abundant research results on rock unloading mechanical properties, the application of NMR technology in the rock field and the establishment of a damage model. However, there are relatively few studies combining NMR technology with an unloading test to analyze the changes in saturated rock fracture structure and the characteristics of mechanical parameters at the same time. The complex meso fracture structure in rock leads the damage evolution process and deformation and failure of rock and determines the macro mechanical properties and failure characteristics of the rock. The meso damage of rock is manifested as the change of pore and the expansion of rock fracture. The change in the distribution of porosity and pore size reflects the meso damage of rock. In this paper, the sandstone in the strong aquifer of a mine in Zigong, Sichuan was taken as the research object, and the NMR test system was used to carry out the saturated rock unloading mechanical test, to study the change characteristics of rock porosity and T_2 spectrum curves under different stress unloading conditions, quantitatively analyze the generation, expansion and penetration process of rock internal fractures, analyze the change of rock internal fracture structure and meso damage evolution law, and establish the damage model suitable for rock NMR law based on the damage theory. The research results provide experimental data for the study of the damage mechanism of unload rock mass, and have important reference significance for solving engineering geological problems in a similar geological environment (such as confining pressure unloading instability process in goaf, excavation failure of water-rich engineering rock mass, etc.).

2 Test Principle and Procedure

### 2.1 Samples Preparation and Test Equipment

The test rock samples were taken from the sandstone at a depth of 40 m in a mine in Zigong, Sichuan Province. Most of the mining area is a semi-hard rock formation, which is composed of the sand and mudstone of the Shaximiao Formation of the Jurassic system. The sandstone accounts for about one-third. The structure of sandstone is fine-grained, mostly argillaceous cementation and hard. The climate in the sampling project area is warm and humid, and the surface drainage is relatively developed. The development depth of shallow freshwater in the area is more than 100 m. The aquifer where the sampling site is located is mainly sandstone, with abundant fresh water, which has a certain impact on the construction excavation. According to the "code for rock test of water conservancy and hydropower engineering", the rock is processed into a standard cylindrical sample with a diameter of 50 mm and a height of 100 mm (Fig. 1). Samples with uniform apparent distribution, similar quality, height, diameter, longitudinal wave velocity, initial porosity and T_2 spectrum distribution are selected from a batch of rock samples for test. The uniaxial compressive strength of the rock in the dry state is 76.98 MPa, and the basic mechanical property data in the saturated state are shown in Table 1. The testing machine and loading rate used in the uniaxial and triaxial tests are the same as the subsequent unloading tests. The relevant parameters are as follows: the confining pressure loading rate is 0.1 MPa/s; The axial pressure loading rate is 0.25 MPa/s.

Fig. 1 Sandstone samples

Table 1 Conventional mechanical parameters of saturated sandstone

Rock type	Sample state	Density (g/cm^3)	Uniaxial compressive strength/Mpa	Triaxial compressive strength under 20 MPa confining pressure /MPa	Elastic modulus / GPa	Poisson's ratio	Porosity/%
Sandstone	Water saturated	2.475	63.32	169.44	27.21	0.27	5.47
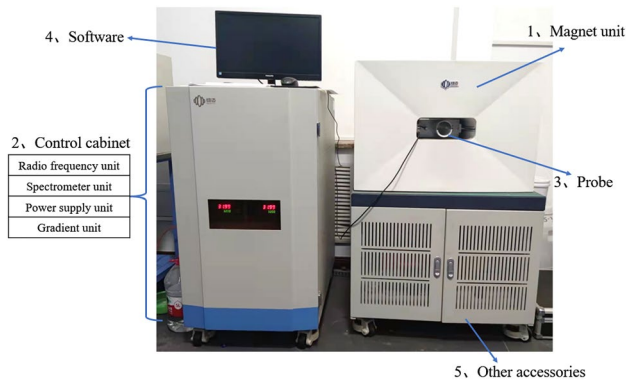
Fig. 2 MesoMR23-060H-I NMR test system

The main experimental instruments used in the test are ZYB-II vacuum pressure saturation device, which is used to saturate the rock to achieve full saturation; mesoMR23-060H-I core NMR analyzer (Fig. 2), used to analyze porosity and pore size distribution; rock 600-50 VHT rock high temperature triaxial rheological test system (Fig. 3), can accurately control the rock loading rate, real-time recording of stress and strain deformation.

2.2 NMR Testing Principle

NMR is the interaction between the atomic nucleus and magnetic field. The relaxation characteristics of water in rock pores are measured by the interaction between the magnetism of H atomic nucleus rich in water in saturated rock and magnetic field (Martini et al. 2018). Due to the different pore size and pore water content in each rock, the speed of releasing energy is also different. According to the difference in signals, the T_2 distribution and signal intensity curves of different transverse relaxation times can be obtained. The T_2 relaxation time curve can reflect the variation characteristics of cracks, pore size, pore number and pores in rock samples. There are three different relaxation mechanisms for fluids in rock pores: free relaxation, surface relaxation and diffusion relaxation, which can be expressed by the following formula (Zhou et al. 2014a, b, 2018a, b):

$$\frac{1}{T_2} = \frac{1}{T_{2f}} + \frac{1}{T_{2s}} + \frac{1}{T_{2d}} \tag{1}$$

where T_2 is the relaxation time; T_{2f} is the transverse relaxation time of pore fluid in a sufficiently large container; T_{2s} is the transverse relaxation time caused by surface relaxation of pore fluid; T_{2d} is the transverse relaxation time of pore fluid caused by diffusion under magnetic field gradient.

When the rock sample is fully saturated, the free relaxation and diffusion relaxation are much less than the surface relaxation. The T_2 value of the rock is determined by the surface relaxation. The relationship between T_2 and pores is as follows:

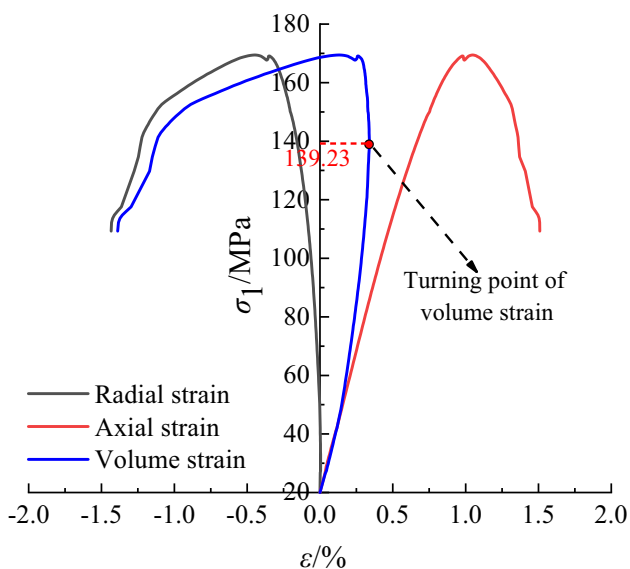**Fig. 3** Rock 600–50 VHT high temperature triaxial rheological test system
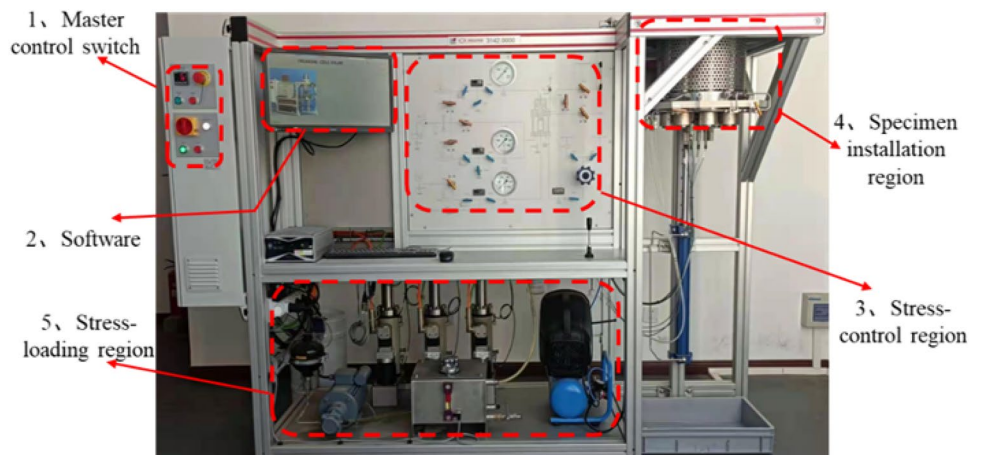
Fig. 4 Stress–strain curve of rock sample under triaxial compression test

Fig. 5 Stress loading path

$$\frac{1}{T_2} \approx \frac{1}{T_{2s}} = \rho_2 \frac{S}{V} = F_s \frac{\rho_2}{r} \tag{2}$$

where ρ_2 is the surface relaxivity, taken as 30 μm/s; S is the pore surface area; V is the fluid volume; F_S is the geometric factor. F_S is taken as 3 for spherical pores and 2 for cylindrical pipes; R is the pore radius, μm.

According to Eq. (2), T_2 spectrum can reflect the distribution of pore radius of rock, and the relationship curve between porosity and pore radius r can be transformed into the relationship curve with relaxation time T_2, so as to establish the relationship between relaxation time T_2 and pore radius R.

2.3 Test Methods

Conventional triaxial stress–strain curves of rock under 20 MPa confining pressure are shown in Fig. 4. To study the unloading damage evolution law of rock under different initial axial compression conditions, the initial stress state of rock is characterized by the percentage of initial axial compression in triaxial compressive strength (TCS). According to the conventional triaxial stress–strain curves under 20 MPa confining pressure, the volumetric strain rotation point of the rock is near 80% TCS. To minimize the influence of initial axial pressure and confining pressure on a rock in the loading stage, the initial axial pressure is set as 70%, 80% and 90% of TCS to characterize three different initial axial pressures. At the same time, to analyze the different stages of rock unloading, the unloading confining
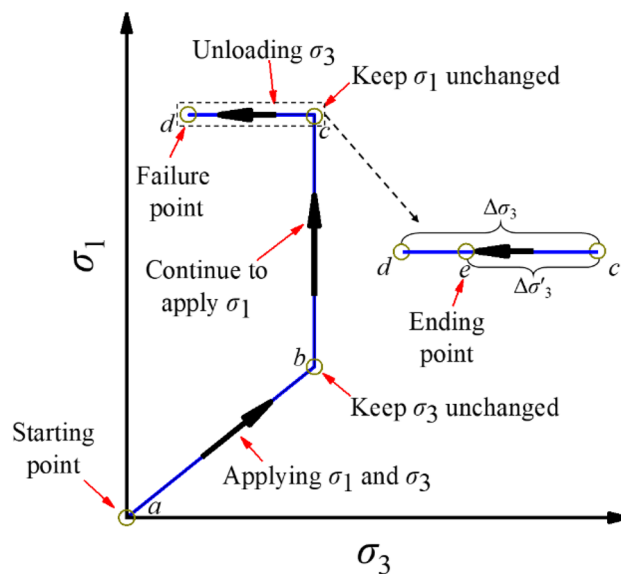
pressure ratio K is proposed as a descriptive variable, which is expressed as:

$$K = \frac{\Delta\sigma_3'}{\Delta\sigma_3} \tag{3}$$

where $\Delta\sigma_3'$ is the unloading confining pressure value of the rock sample from the initial confining pressure, MPa; $\Delta\sigma_3$ is the unloading confining pressure value of the rock sample from the initial confining pressure unloading to the unloading failure point, MPa.

The main test steps are as follows:

1. At the beginning of the test, the ZYB-II vacuum pressure saturation device is used to vacuum pressurize and water the rock. The pressure value is 25 MPa and the water saturation time is 24 h. After the sample is saturated with water, take it out for test;

2. The Rock 600-50 VHT rock high temperature triaxial rheological test system is used to carry out conventional triaxial unloading tests with different initial axial pressure and different unloading confining pressure ratio. Firstly, apply the axial pressure and confining pressure to the predetermined value of 20 MPa at the same time. When the confining pressure reaches 20 MPa, continue to load the axial pressure to the predetermined value of axial pressure, and then keep the axial pressure constant and unload the confining pressure to the failure or predetermined value (Fig. 5). To reduce the impact of loading and unloading rate on the test results, the loading and

Table 2 Unloading confining pressure of each rock sample

Group	Rock sample number	Axial compression/MPa	Initial confining pressure/MPa	Final confining pressure/MPa	$\Delta\sigma'_3$/MPa	$\Delta\sigma_3$/MPa	Unloading confining pressure ratio/%
Group A	A-0	118.61	20	20	0	13.53	0
	A-1	118.61	20	13.24	6.77	13.53	50
	A-2	118.61	20	9.85	10.15	13.53	75
	A-3	118.61	20	7.82	12.18	13.53	90
	A-4	118.61	20	6.47	13.53	13.53	100
Group B	B-0	135.55	20	20	0	9.28	0
	B-1	135.55	20	15.36	4.64	9.28	50
	B-2	135.55	20	13.04	6.96	9.28	75
	B-3	135.55	20	11.65	8.35	9.28	90
	B-4	135.55	20	10.72	9.28	9.28	100
Group C	C-0	152.5	20	20	0	6.8	0
	C-1	152.5	20	16.6	3.4	6.8	50
	C-2	152.5	20	14.9	5.1	6.8	75
	C-3	152.5	20	13.88	6.12	6.8	90
	C-4	152.5	20	13.2	6.8	6.8	100

unloading rate of this test remains uniform, and the relevant parameters are as follows: the confining pressure loading rate is 0.1 MPa/s, and the confining pressure unloading rate is 0.05 MPa/s; The axial pressure loading rate is 0.25 MPa/s and the axial pressure unloading rate is 0.25 MPa/s.

3. Divide the rock samples into three groups, numbered A, B and C. Apply axial pressure to 70%, 80% and 90% of TCS according to the above steps, and unload the confining pressure until the sample is damaged to obtain the value of $\Delta\sigma_3$. Calculate the required unloading confining pressure $\Delta\sigma'_3$ and final confining pressure (Table 2) when K is 0%, 50%, 75%, 90% and 100%, respectively

After loading the initial axial and confining pressure on each rock sample according to the above scheme, unload the confining pressure to the predetermined confining pressure value, then keep the confining pressure unchanged, unload the axial pressure to equal to the confining pressure gradually, then unload the axial pressure and confining pressure to 0 MPa at the same time, and take out the sample.

4. The MesoMR23-060H-I NMR test system is used to test the rock samples under different unloading conditions, and the porosity and NMR relaxation time curves of the rock samples after unloading are obtained (Fig. 6).
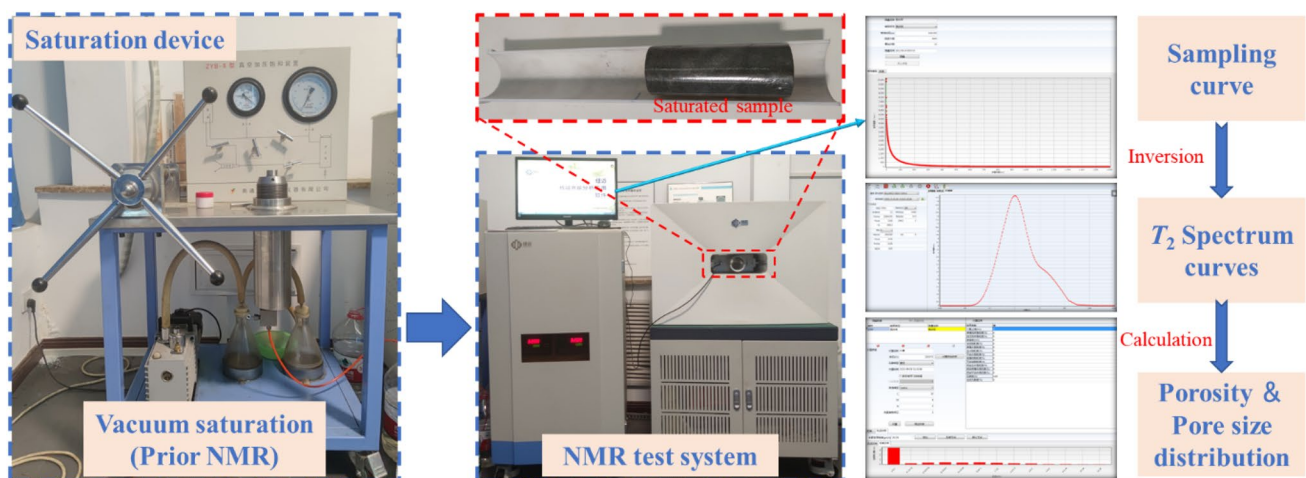

Fig. 6 NMR test flow

3 Analysis of Test Results

## 3.1 Analysis of Mechanical Test Results

3.1.1 Stress–Strain Curve

The relationship curve between load and deformation (stress–strain curve) obtained by compressing standard rock samples with a testing machine can reveal the variation law of rock mechanical properties. The stress–strain curves of unloading test of multiple groups of samples are shown in Fig. 7, with radial strain on the left and axial strain on the right.

Due to the simultaneous loading confining pressure and axial pressure to the predetermined value at the same time, the sample is compressed to a relatively dense state under the action of pressure, while the stress–strain curve in Fig. 7 corresponds to that after confining pressure loading, so it can not reflect the pore compression stage. The stress–strain curve is mainly divided into three stages: Elastic deformation stage, the stress–strain curve increases linearly and the rock deformation is stable. Plastic deformation stage, the sample begins to yield, the stress–strain curve changes from a straight line to convex, and the cracks in the rock begin to sprout and expand rapidly. Crack instability propagation stage (failure stage), the sample expands and deforms unsteadily, and the stress–strain curve shows a small drop. This was due to the reduction of the confining pressure, which caused the sample stress to be uneven and difficult in maintaining the axial stress. The stress–strain curve decreased sharply when the unloading failure occurred, manifesting as a brittle failure. By observing the stress–strain curve, it can be found that the axial strain curve before unloading is approximately a straight line, while the radial strain curve shows obvious bending, indicating that the rock is in the stage of elastic deformation and weak plastic deformation, and the axial strain curve of different initial axial pressures are significantly different. According to Fig. 7a~c, the axial strain curve before unloading under 70% TCS is almost a straight line, showing obvious elastic deformation, that is, the rock does not enter the plastic deformation stage before unloading under 70% TCS. With the increase of the initial axial stress level, the convex characteristics of the axial strain curve before unloading are more obvious, the axial strain curve under 80% TCS shows slight plastic deformation before unloading, and the plastic deformation under 90% TCS is the most obvious. In the process of axial compression loading, the changing trend of the axial strain curve is much greater than that of radial strain. When the axial pressure is less than 60 MPa, the radial strain hardly changes, indicating that the rock is in the process of elastic
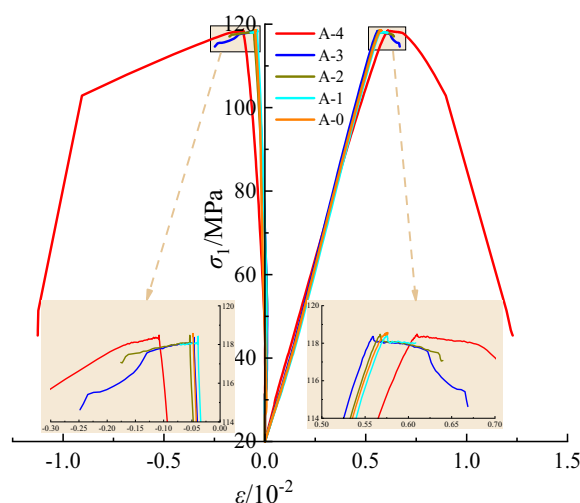
(a) Unloading stress-strain curve under 70% TCS
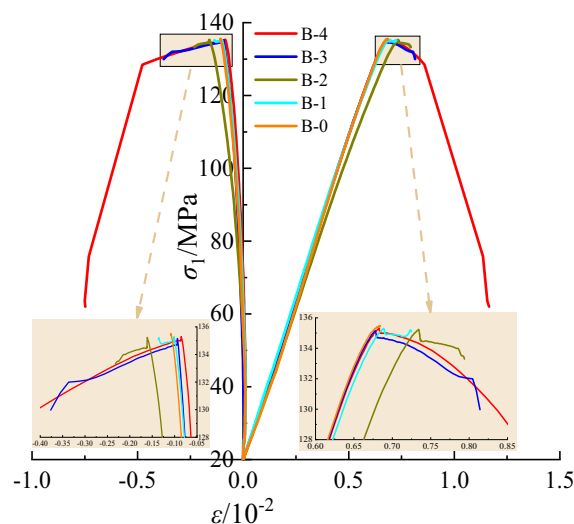
(b) Unloading stress-strain curve under 80% TCS
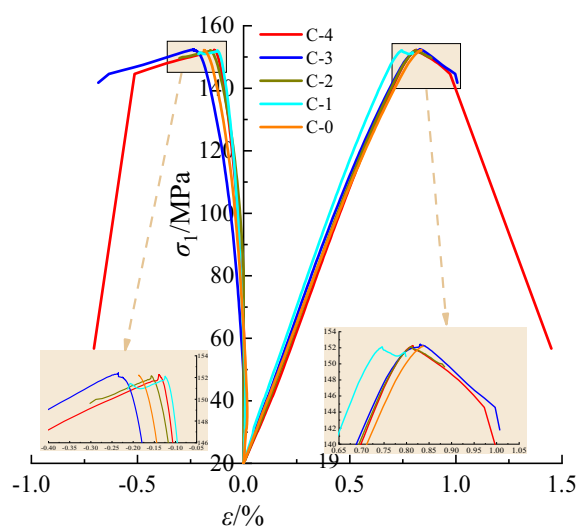
(c) Unloading stress-strain curve under 90% TCS

Fig. 7 Stress–strain curve of unloading test

compression and basically does not produce new cracks. When the axial pressure exceeds 60 MPa, the radial strain begins to increase gradually, indicating that the rock expands gradually, the originally compressed pores gradually recover or expand slightly, and a certain number of new cracks are generated. In the unloading stage, the variation range of radial strain is more obvious, and the rock begins to enter the plastic deformation stage. In the micro view, the internal crack is expanding, macroscopically, it is characterized by dilatancy.

3.1.2 Elastic Modulus and Poisson's Ratio

The mechanical parameters of rock, such as elastic modulus and Poisson's ratio, are calculated according to the elastic deformation stage of rock. When analyzing the mechanical parameters of rock in the unloading stage, it is necessary to consider the influence of stress and strain in different stress directions. It is assumed that all points of stress and strain in the unloading process comply with generalized Hooke's law. The calculation formula for mechanical deformation parameters of rock is as follows (Zhou et al. 2018a):

$$E = (\sigma_1 - 2\mu\sigma_3)/\varepsilon_1$$
$$\mu = (B\sigma_1 - \sigma_3)/[(2B - 1)\sigma_3 - \sigma_1] \quad (4)$$
$$B = \varepsilon_3/\varepsilon_1$$

where E is the deformation modulus, μ is Poisson's ratio, σ_1 is axial pressure, σ_3 is confining pressure, ε_1 is axial strain, ε_3 is the radial strain and B is the radial expansion coefficient.

Table 3 shows the mechanical parameters corresponding to the unloading termination point of the sample, where ε_v is the volume strain at the unloading termination point, and U is the total energy absorbed by the rock at the unloading termination point.

Under different initial axial pressures, with the increase of unloading confining pressure ratio, the ε_v and E decrease gradually, and U and μ increase gradually. Under 70%, 80% and 90% TCS, when the unloading confining pressure ratio increases from 0 to 100%, the increased range of U is 114.78%, 80.25% and 83.25%, respectively. According to the variation law of mechanical parameters, both unloading confining pressure ratio and initial axial pressure have a great influence on the rock. In the early stage of unloading, the increase of initial axial pressure has a more significant impact on the rock, while in the late stage of unloading, the change of confining pressure has a more significant impact.

Figure 8 shows the change trend of elastic modulus and Poisson's ratio at the end of unloading. With the increase of the unloading confining pressure ratio, the elastic modulus at the unloading termination point decreases until the unloading failure reaches the lowest value. Under different initial axial pressures, the change trend of rock elastic modulus is basically the same. The greater the initial axial pressure, the smaller the elastic modulus at the same unloading point, indicating that the larger initial axial pressure promotes rock deterioration. When the unloading confining pressure ratio is less than 90%, the elastic modulus decreases slowly, the rock is in the stage of elastic–plastic deformation, cracks are constantly generated in the rock, but the whole remains intact. When the unloading confining pressure ratio is greater than 90%, the elastic modulus decreases significantly and the rock is in the stage of instability and failure. Brittle failure of rock occurs, which is manifested as dilatancy, and the mechanical parameters change suddenly after rock failure. Under

| Table 3 Rock unloading mechanical parameters	Group	Rock sample number	$\varepsilon_1/10^{-2}$	$\varepsilon_3/10^{-2}$	$\varepsilon_v/10^{-2}$	μ	E/GPa	U/(MJ·m^{-3})
	Group A	A-0	0.576	− 0.045	0.485	0.207	19.131	0.381
		A-1	0.609	− 0.061	0.486	0.188	18.568	0.408
		A-2	0.640	− 0.157	0.327	0.292	17.396	0.424
		A-3	0.669	− 0.227	0.216	0.365	16.283	0.453
		A-4	1.228	− 1.126	− 1.023	0.757	2.914	0.818
	Group B	B-0	0.684	− 0.108	0.468	0.256	18.309	0.498
		B-1	0.725	− 0.137	0.452	0.260	17.564	0.553
		B-2	0.794	− 0.232	0.329	0.336	15.735	0.586
		B-3	0.814	− 0.377	0.061	0.471	14.697	0.611
		B-4	1.165	− 0.748	− 0.331	0.587	4.322	0.898
	Group C	C-0	0.777	− 0.187	0.403	0.312	17.981	0.661
		C-1	0.799	− 0.213	0.372	0.322	17.559	0.696
		C-2	0.884	− 0.302	0.280	0.378	15.638	0.704
		C-3	1.007	− 0.685	− 0.363	0.632	12.323	0.817
		C-4	1.450	− 0.705	0.040	0.493	3.064	1.219
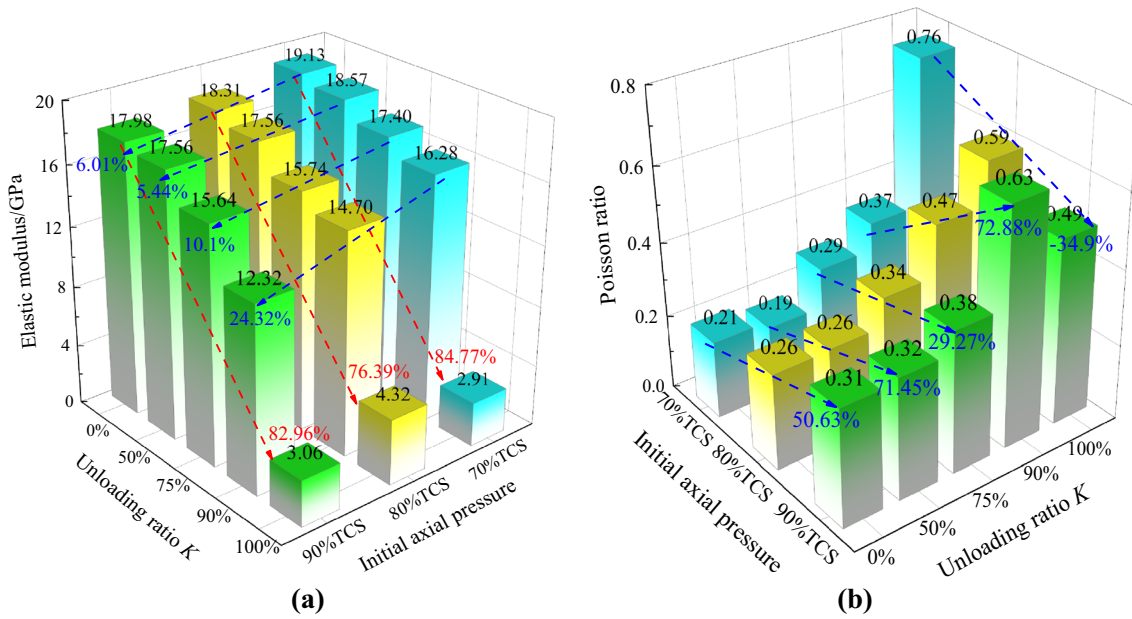
Fig. 8 **a** Change trend of elastic modulus, **b** change trend of Poisson's ratio

70%, 80% and 90% TCS, when the unloading confining pressure ratio increases from 0 to 100%, the reduction range of elastic modulus is 84.77%, 76.39% and 82.96%. Under 70% TCS, the elastic modulus of rock decreases the most. This is because when a failure occurs, the dilatancy phenomenon is the most obvious, and the radial strain is the largest, which has a great impact on the reduction of elastic modulus.

The changing trend of Poisson's ratio basically increases with the increase of the unloading confining pressure ratio.

When the unloading confining pressure ratio is less than 90%, at the same unloading point, the greater the initial axial pressure, the greater the Poisson's ratio. The difference in initial axial pressure has a greater impact on the deformation of rock at this stage. Under 90% TCS, the Poisson's ratio of 90% unloading confining pressure ratio exceeds 0.5, indicating that the rock is seriously damaged and deformed at this point and is close to failure. From 90% unloading confining pressure ratio to unloading
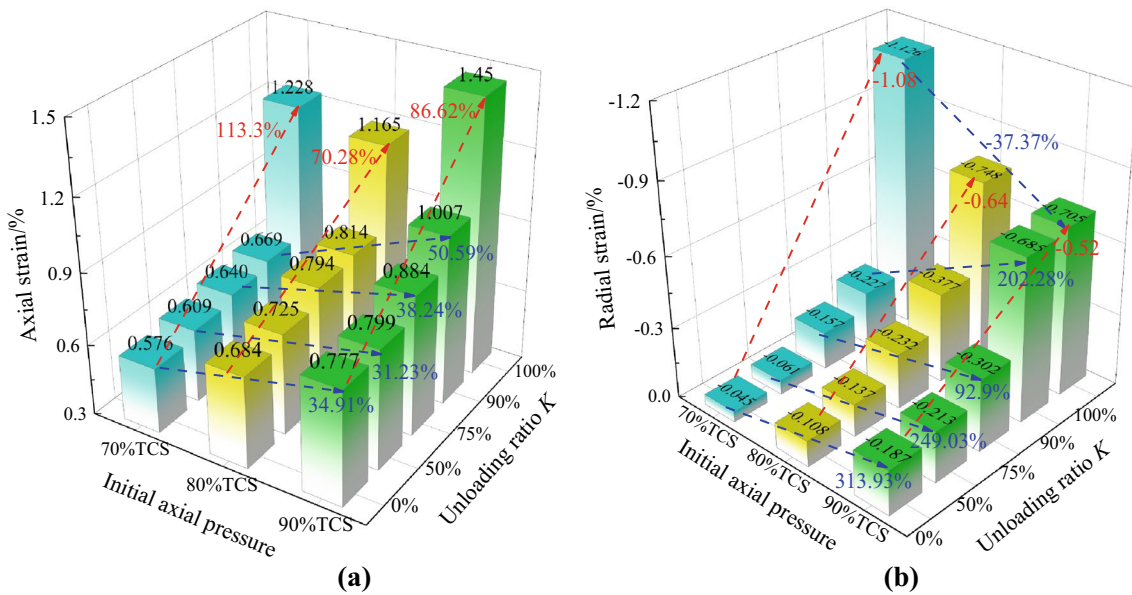

Fig. 9 **a** Variation trend of axial strain, **b** variation trend of radial strain

failure point, Poisson's ratio decreases, which is caused by the fact that the axial strain increment of rock is much greater than the radial strain and the radial expansion coefficient decreases. When the unloading reaches the failure point, the Poisson's ratio shows the opposite trend. The larger the initial axial pressure is, the smaller the Poisson's ratio is. This is because under the condition of low axial pressure, the confining pressure from 90% unloading confining pressure ratio to the failure point is greater, and the radial strain increment is greater. Under high axial pressure, the axial stress is greater, and the axial strain increment is greater, so the Poisson's ratio at the unloading failure point under low axial pressure is greater.

3.1.3 Strain Characteristics

Figure 9 shows the axial and radial strain variation trend at the unloading termination point. During the unloading process, the axial strain, radial strain and volume strain at the unloading termination point increase with the unloading confining pressure ratio, and the variation trend is basically the same between different initial axial pressures. The larger initial axial pressure promotes the growth of strain. At the same unloading point, the axial strain and radial strain of rock increase with the increase of initial axial pressure, and the volumetric strain decreases. When unloading failure occurs, the deformation in the radial direction under low initial axial compression is larger, and the expansion phenomenon is more obvious. By comparing and observing the strain changes of samples A-4, B-4 and C-4, the axial and radial strains at the unloading termination point increase sharply, and the volumetric strain changes to a negative value. The rock unloading failure shows the expansion characteristics. The larger the initial axial pressure, the larger the axial strain value and the smaller the radial strain value when the unloading failure occurs. The main reason is that under high initial axial pressure, the rock has reached the state of near failure before unloading failure, while under low initial axial pressure, the degree of rock damage before failure is relatively small, and the internal damage of the rock will increase sharply when it reaches failure. At the same time, the unloading confining pressure at the unloading failure point under low axial pressure is greater. The retained confining pressure at the unloading failure point under high axial pressure is large, and the mutation effect of rock failure will be restrained by confining pressure, so the capacity expansion phenomenon is more obvious under low axial pressure.

In the stage of unloading confining pressure ratio of 0~50%, the strain increment at the unloading termination point is small and no large deformation occurs, indicating that the rock is mainly in the stage of elastic deformation. In the stage of unloading confining pressure ratio of 50~90%,

the increased range of axial strain is still small. The strain change range of the sample is the largest under 90% TCS and the smallest under 70% TCS, while the change range of radial strain and volumetric strain increases rapidly at this stage. Under larger initial axial compression, the increase of radial strain and the decrease of volumetric strain are larger, and the sample began to transform from elastic deformation to plastic deformation. When the unloading confining pressure ratio exceeds 90%, the strain at the unloading termination point changes greatly. At this stage, the internal crack of the rock enters the unstable propagation stage, the crack expands rapidly, the macro fracture surface is gradually formed, and the degree of rock damage increases sharply.

3.2 Energy Dissipation Characteristics

3.2.1 Quantitative Characterization of Energy Dissipation

The generation and propagation of microcracks in rock are accompanied by energy consumption. Therefore, the deformation and failure process of rock is a complex energy transformation process, and the dissipation reflects the attenuation degree of the original strength of the rock. It is known from the first law of thermodynamics that there is no heat exchange between physical process changes of matter within a closed system and the outside world. In other words, the rock sample and the testing machine are regarded as a closed system, and the rock sample unit is deformed and damaged under the action of the testing machine. There is an energy exchange between the testing machine and the rock sample unit, but there is no energy exchange with the outside world. According to the law of thermodynamics, the total energy U input by
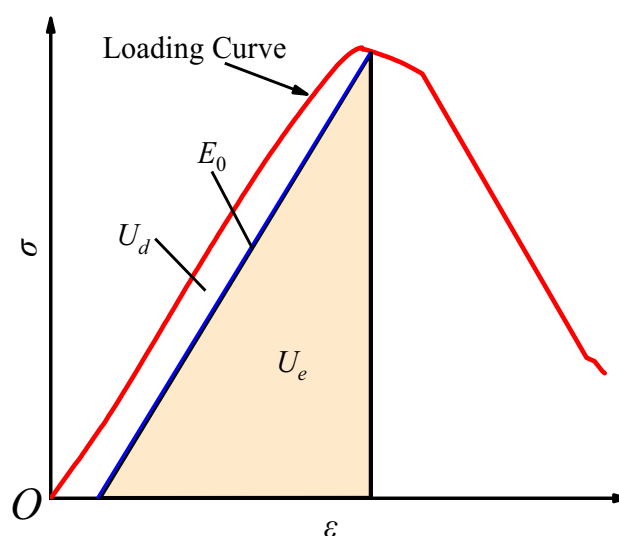
Fig. 10 Calculation relationship between dissipated energy and elastic

external work is converted into the internal releasable elastic strain energy U_e and unit dissipation energy U_d of the rock sample(Wen et al. 2019; Xie et al. 2009), that is:

$$U = U_e + U_d \tag{5}$$

where U is the total energy generated by work done by an external force, and U_e is the elastic strain energy; U_d is the dissipated energy, which is used to form the internal damage and deformation of a rock sample.

The calculation relationship between elastic energy and dissipation energy is shown in Fig. 10.

In the triaxial loading and unloading path test, both axial pressure and confining pressure work on the rock sample. Therefore, the total energy absorbed by the rock sample includes the positive work of axial stress on the rock sample, the positive work of confining pressure when the radial deformation of the rock sample increases positively, and the negative work of confining pressure on the rock sample when the radial deformation of the rock sample increases negatively (Zhang et al. 2021a, b):

$$U = U_1 + 2U_3 \tag{6}$$

where U_1 is the axial strain energy generated by the axial deformation of the rock sample, which is generally positive; U_3 is the radial strain energy generated by the radial deformation of the rock sample, which is generally positive in the initial stage of the test and turns to negative as the test progresses.

The calculation formulas of U_1 and U_3 are as follows:

$$U_1 = \int \sigma_1 d\varepsilon_1 \tag{7}$$

$$U_3 = \int \sigma_3 d\varepsilon_3 \tag{8}$$

The calculation formula of elastic energy under triaxial compression is:

$$
\begin{aligned}
U_e &= \frac{1}{2E_r}\left[\sigma_1^2 + 2\sigma_3^2 - 2\mu\left(2\sigma_1\sigma_3 + \sigma_3^2\right)\right] \\
&\approx \frac{1}{2E_0}\left[\sigma_1^2 + 2\sigma_3^2 - 2\mu\left(2\sigma_1\sigma_3 + \sigma_3^2\right)\right]
\end{aligned} \tag{9}
$$

When calculating, take the initial elastic modulus E_0 instead of E_r.

3.2.2 Analysis of Energy Dissipation Law

To compare the change of each energy of the sample at the unloading termination point under different unloading confining pressure ratios and different initial axial compression conditions, only the energy state of the sample at the unloading termination point was analyzed here. According to the above energy calculation formula, the changes of total energy, elastic energy and dissipated energy at the completion of the test under different unloading confining pressure ratio can be obtained, as shown in Fig. 11, and the fitting function and correlation coefficient of each energy are shown in Table 4.

Under each initial axial pressure, with the change of unloading confining pressure ratio, the corresponding energy change trend characteristics are basically the same. In the process of loading and unloading, the axial strain energy U_1 is much larger than the radial strain energy U_3. Under 70%, 80% and 90%TCS, when the unloading confining pressure ratio increases from 0 to 100%, U_1 increases by 153.13%, 99.26% and 94.32%, and U_3 increases by 910.56%, 313.64% and 186.62%, respectively. The larger the initial axial pressure, the smaller the increase of U_1 and U_3. Because the greater the initial axial pressure, the greater the initial strain energy, the smaller the corresponding increase. When the unloading confining pressure ratio is less than 90%, U_1 and U_3 show steady linear growth, and the rock samples are mainly in the stage of elastic deformation. In the stage of 90~100% unloading confining pressure ratio, U_1 and U_3 show abrupt growth, and the rock samples are in the stage of plastic deformation. Under 90% TCS, the increment of radial strain energy value is small in the stage of 90~100% unloading confining pressure ratio, indicating that under 90% TCS, when the unloading confining pressure ratio is 90%, the radial deformation of rock is serious and is on the verge of failure. Therefore, when the unloading failure occurs, the increment of radial strain is small.

It can be seen from Fig. 11b that with the increase of the unloading confining pressure ratio, the total energy absorbed by the sample under each initial axial pressure increases monotonically. And the changing trend coincides with the changing height of U_1, indicating that the total energy mainly depends on the change of axial strain energy, while the change of radial strain energy has little effect on the total energy. Under 70% TCS, 80% TCS and 90% TCS, when unloading failure occurred, the total energy absorbed is 0.818 MJ·m^{-3}, 0.898 MJ·m^{-3} and 1.211 MJ·m^{-3}, respectively. Compared with the beginning of unloading, the increase in total energy is 114.78%, 80.25% and 83.25%, respectively. In the stage of 0~90% unloading confining pressure ratio, the change of total energy is small. In this stage, different initial axial pressure has a greater impact on the change of total energy. At the same unloading point, the greater the initial axial pressure, the greater the total energy increases significantly. The total energy in the stage of 90~100% unloading confining pressure ratio increases sharply, which is mainly due to the failure of the sample and the sharp increase of strain, resulting in a large increase of energy.
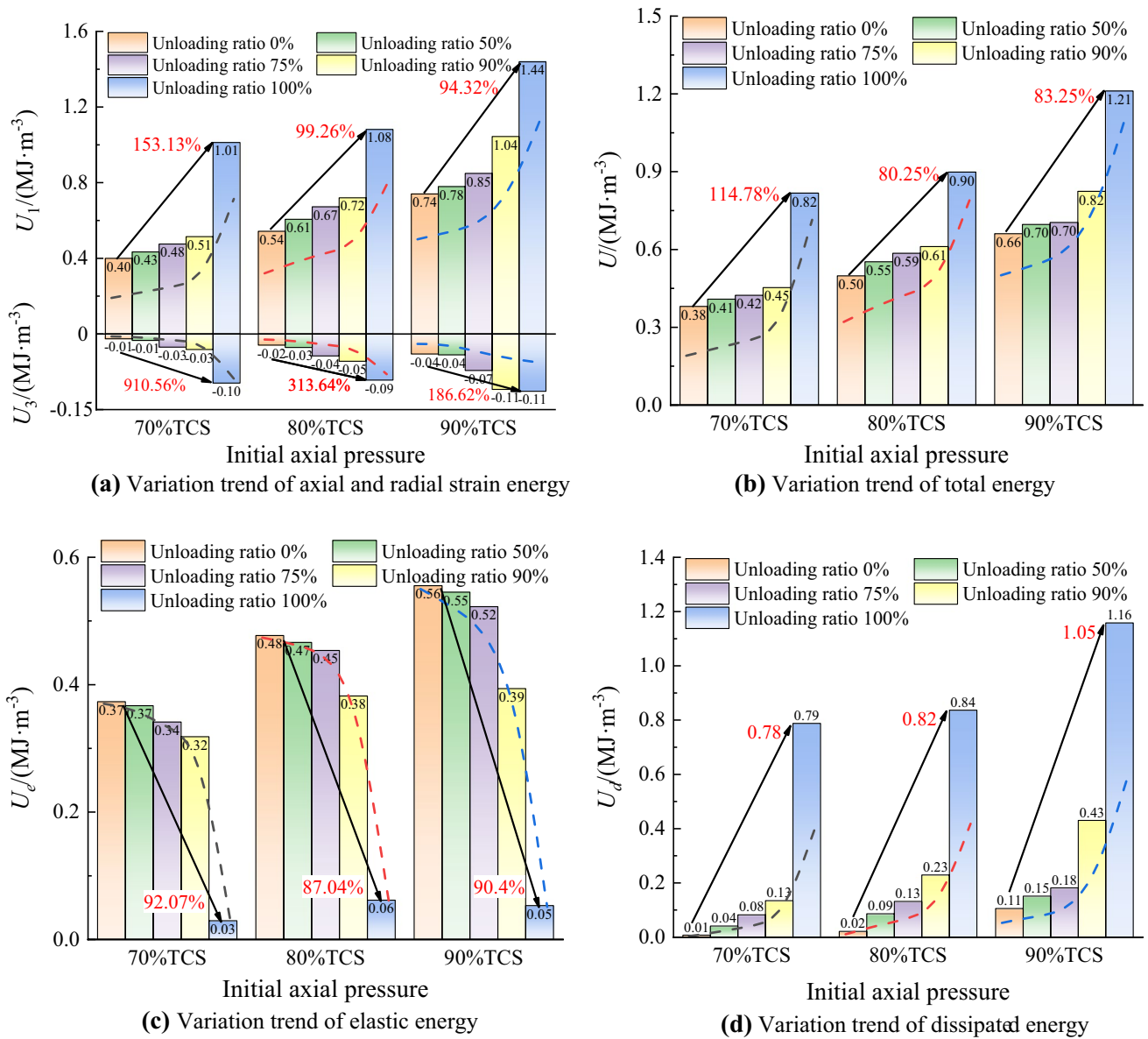
(a) Variation trend of axial and radial strain energy

(b) Variation trend of total energy

(c) Variation trend of elastic energy

(d) Variation trend of dissipated energy

Fig. 11 Variation law of energy

With the increase of unloading confining pressure ratio, the elastic energy gradually decreases and its proportion decreases, the dissipated energy gradually increases and its proportion increases. When the unloading confining pressure ratio is less than 90%, most of the energy input by external work is transformed into elastic energy, and the other part is transformed into dissipative energy, which is used for the development of micro fractures and deformation in rock samples. Under 70%, 80% and 90% TCS, the proportion of elastic energy under the unloading confining pressure ratio of 0% and 90% is 98.05%, 95.71%, 84.02%, 70.26%, 62.53% and 47.78%, respectively. Large initial axial pressure accelerates the fracture development and deformation degree of

the sample, and the rock will turn into plastic deformation earlier. In the stage of 90~100% unloading confining pressure ratio, the elastic energy decreases sharply and the dissipated energy increases sharply. The propagation of cracks in the sample shows a mutation character. The micro-cracks penetrate to form a failure surface and the rock sample failure occurred. At this time, the stored elastic strain energy is greatly reduced and converted into dissipated energy, and a small part of the remaining elastic energy is stored in the rock sample. After the failure of the sample, the proportion of elastic energy under 70% TCS, 80% TCS and 90% TCS is only 3.62%, 6.25% and 4.4%, respectively.

Table 4 Energy fitting relationship

| Energy category	Initial axial pressure	Energy fitting relationship	R^2
U_1	70% TCS	$U_1 = 9.519 \times 10^{-4} K + 0.397 + \exp(0.278 K\text{-}28.417)$	0.99935
	80% TCS	$U_1 = 1.64 \times 10^{-3} K + 0.538 + \exp(0.24 K\text{-}24.972)$	0.99818
	90% TCS	$U_1 = 6.732 \times 10^{-4} K + 0.74 + \exp(0.095 K\text{-}9.994)$	1
U_3	70% TCS	$U_3 = -1.481 \times 10^{-2} - \exp(0.15 K\text{-}17.513)$	0.9759
	80% TCS	$U_3 = -2.374 \times 10^{-2} - \exp(0.061 K\text{-}8.846)$	0.97905
	90% TCS	$U_3 = -3.023 \times 10^{-2} - \exp(0.0297 K\text{-}5.372)$	0.93822
U	70% TCS	$U = 5.654 \times 10^{-4} K + 0.381 + \exp(0.287 K\text{-}29.681)$	1
	80% TCS	$U = 1.15 \times 10^{-3} K + 0.498 + \exp(0.332 K\text{-}34.421)$	0.99969
	90% TCS	$U = 4.772 \times 10^{-4} K + 0.664 + \exp(0.146 K\text{-}15.334)$	0.99928
U_e	70% TCS	$U_e = 0.362 - \exp(0.197 K\text{-}20.836)$	0.99414
	80% TCS	$U_e = 0.469 - \exp(0.152 K\text{-}16.14)$	0.99906
	90% TCS	$U_e = 0.551 - \exp(0.115 K\text{-}12.197)$	0.99979
U_d	70% TCS	$U_d = 9.373 \times 10^{-4} K + 4.19 \times 10^{-3} + \exp(0.27 K\text{-}27.359)$	0.99964
	80% TCS	$U_d = 1.4 \times 10^{-3} K + 0.02 + \exp(0.21 K\text{-}21.36)$	0.99994
	90% TCS	$U_d = 6.292 \times 10^{-4} K + 0.109 + \exp(0.133 K\text{-}13.267)$	0.99972

3.3 Pore Characterization Analysis

3.3.1 T_2 Spectrum Curve of Relaxation Time

The distribution of T_2 spectrum curve can reflect the size information of pores and the quantity information of pores with different sizes in rock. According to the relaxation time of hydrogen atom in water, the state of the pore can be reflected. The longer the relaxation time, the smaller the binding of the water molecule and the larger the pore size. On the contrary, the binding of the water molecule is large and the pore size is small, that is, the size of T_2 value is positively correlated with the pore size (Zhou et al. 2015). The porosity component refers to the percentage of the sum of the pore volume of the corresponding size in the volume of the test sample. The position of the spectral peak is related to the pore size, and the size of the spectral peak area is related to the number of pores and porosity of the corresponding size (Connolly et al. 2019; Nasharuddin et al. 2021). The T_2 spectrum curves of the sample after unloading under different initial axial pressure are shown in Fig. 12.

It can be seen from Fig. 12 that the T_2 spectrum distribution curves of the sandstone sample mainly show three spectrum peaks, the area values of each peak (dimensionless) are quite different, and the area of the peak decreases from the first peak to the third peak, indicating that the pore structure in sandstone is complex after unloading test, and most of the pores are micropores. There is an obvious critical point between the first peak and the second peak. The T_2 spectrum curve is obviously divided into left and right parts by this critical point. The relaxation time corresponding to this critical point is 1.4 ms, after conversion according to Eq. (2), the corresponding aperture is 0.084 μm. That is, the

area of the first peak can be regarded as micropores with a pore diameter less than 0.084 μm, and the area of the second and third peaks can be regarded as mesopores and macropores with a pore diameter bigger than 0.084 μm.

Under different initial conditions, with the increase of unloading confining pressure ratio, the total area and range of T_2 spectrum curve continue to increase, indicating that the pores in the rock continue to develop and the total number of pores continues to increase during unloading. Among them, the area of the first spectral peak always increases with the increase of unloading degree, and the second spectral peak shows the trend of first decreasing and then increasing in varying degrees, which shows that in the unloading process, the number of micropores continues to increase, while the number of mesopores and macropores first decreases and then increases. The reason is that when the rock is in the initial unloading stage of elastic deformation, under the action of initial axial pressure and the tensile stress generated by unloading, pores with smaller pore diameters are constantly generated, and at the same time, mesopores and macropores will be compacted and closed into micropores with smaller pore diameters. In the later stage of unloading, the rock gradually changes from elastic deformation to plastic deformation, the pores of each pore diameter continue to develop and expand, the number of pores continues to increase, the small cracks in the rock expand into macropores gradually, and micropores continue to sprout under the action of load. Under each initial axial pressure condition, before 90% unloading confining pressure ratio, the range of the peak curve basically does not change, the pores expand stably, the increase of the number of micropores is significantly greater than that of mesopores and macropores, and the pore size is basically unchanged, indicating that the
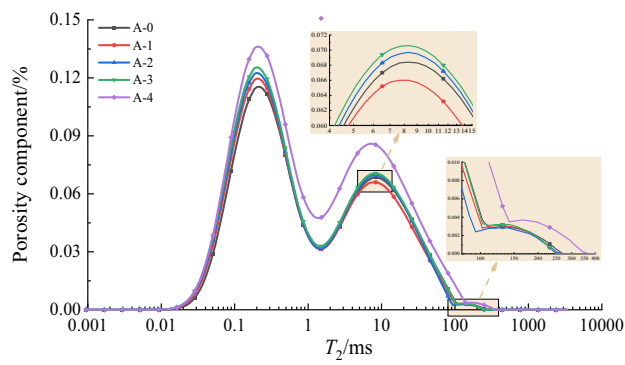
(a) Variation diagram of relaxation time under 70% TCS
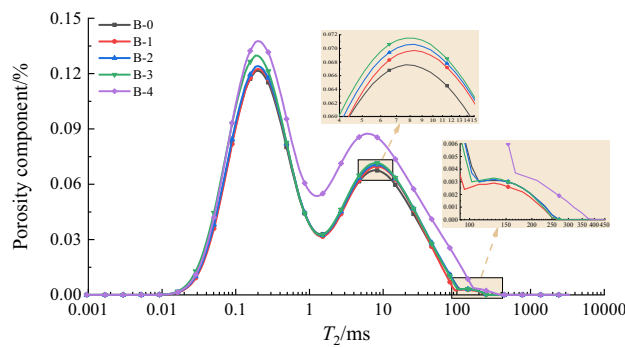
(b) Variation diagram of relaxation time under 80% TCS
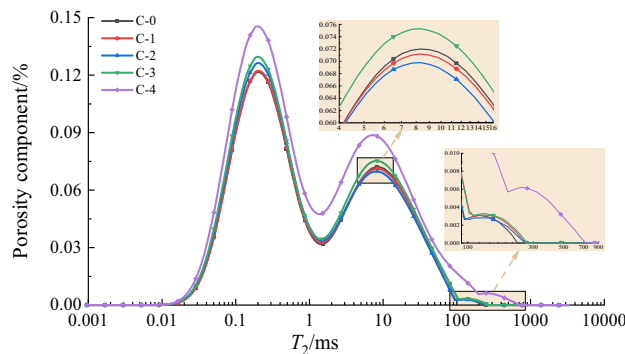
(c) Variation diagram of relaxation time under 90% TCS

Fig. 12 T_2 spectrum curve under different initial axial pressures

damage of the sample at this stage is mainly caused by the continuous increase of the number of internal pores; Compared with the previous curves, the curve of 100% unloading confining pressure ratio increases significantly, and the curve expands significantly to the right. The number of micropores and mesopores and macropores increases rapidly, the pore size also increases, and the pore diameter of macropores increases significantly. Therefore, it can be judged that the damage of the sample is caused by the rapid increase of the number of pores and the rapid development of pore size, the accelerated expansion of macropores and cracks, and the rock damage increases sharply to the maximum value.

In addition, the greater the initial axial pressure, the longer the termination time of T_2 curve spectrum peak when unloading failure occurred, that is, the larger the corresponding maximum pore diameter. Under 70%, 80% and 90% TCS, the maximum internal fracture pore diameter is 22.45 μm, 24.35 μm and 46.54 μm, respectively. It shows that the maximum pore diameter produced in the unloading process of the rock sample is significantly affected by axial pressure. The greater the initial axial pressure is, the more complete the development and destruction of the internal fractures of the rock sample are.

Comprehensive the mechanical test results show that the damage increment and deformation of rock are small before 90% unloading confining pressure ratio, but change sharply after 90% unloading confining pressure ratio, indicating that the increase of pore number has little effect on rock damage and deformation, and the expansion of pore size and the generation of macropores size play a leading role in rock damage, deformation and failure.

3.3.2 Porosity Analysis

The porosity of rock refers to the ratio of all pore volumes in rock to the total volume of rock. The number and size of pores in rock have an important impact on the mechanical properties of rock. NMR porosity measurement was carried out on the samples after the unloading test of each group, and the changes of rock porosity after the test under different initial axial pressure and different unloading confining pressure ratio were obtained, as shown in Fig. 13.

To study the quantitative relationship between porosity and unloading confining pressure ratio under different initial axial pressures, the porosity data are fitted, and the fitting function relationship is as follows:

$$n_{0.7} = 2.56 \times 10^{-3} K + 5.622 + e^{(0.172K - 16.99)} \tag{10}$$

$$n_{0.8} = 1.52 \times 10^{-3} K + 5.854 + e^{(0.173K - 16.9)} \tag{11}$$

$$n_{0.9} = 1.2 \times 10^{-3} K + 5.938 + e^{(0.164K - 15.97)} \tag{12}$$

With the increase of unloading confining pressure ratio, the rock porosity increases exponentially under different initial axial pressures, and the damage degree of samples increases. Before unloading confining pressure, that is, when the unloading confining pressure ratio is 0%, the porosity under 70%, 80% and 90% TCS is 5.64%, 5.87% and 5.94%, respectively. The axial pressure increases from 70 TCS to 90% TCS, and the increase range of rock porosity is 5.32%, indicating that the greater the initial axial pressure, the greater the initial damage degree of rock samples before unloading. Under the unloading confining
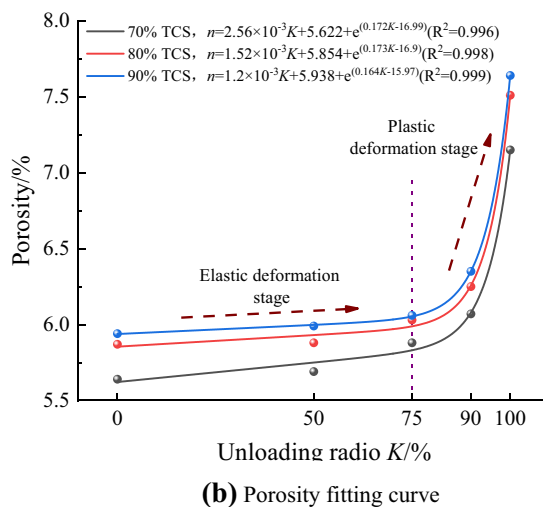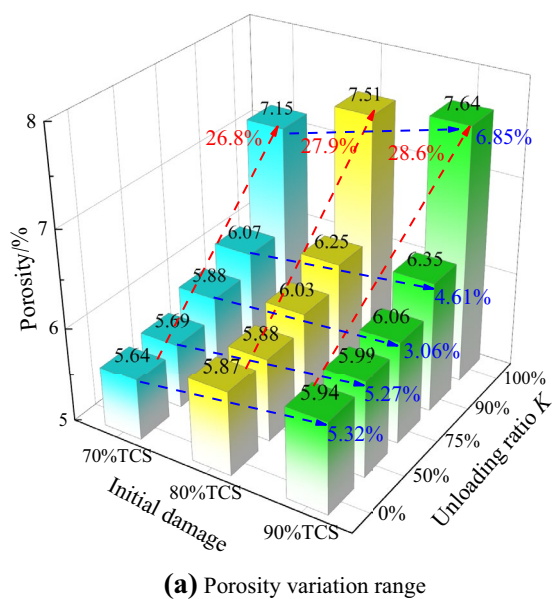
(a) Porosity variation range

(b) Porosity fitting curve

Fig. 13 Variation law of porosity

pressure ratio of 0%, 50%, 75%, 90% and 100%, the axial pressure increases from 70 TCS to 90% TCS, the increment of rock porosity are 0.3, 0.3, 0.18, 0.28 and 0.49, and the increase ranges is 5.32%, 5.27%, 3.06%, 4.61% and 6.85%, respectively. The change shows a trend of decreasing first and then increasing. This is because the unloading confining pressure exerts reverse radial tensile stress on the rock under the action of initial axial pressure. At the same unloading point, under low initial axial compression, the unloading confining pressure and the radial tensile stress are larger. In the initial stage of unloading, the influence of the change of tensile stress caused by unloading confining pressure on rock damage becomes larger gradually, the influence of initial axial pressure on rock damage is weakened, and the difference of rock porosity becomes smaller under different axial pressure; In the later stage of unloading, the rock gradually turns to plastic deformation. The greater the initial axial pressure, the more complete the development of cracks in the rock and the more serious the damage. At this stage, different initial axial pressures have the most significant impact on rock damage. Under 70%, 80% and 90% TCS, when the unloading confining pressure ratio of rock increases from 0 to 100%, the porosity increases by 26.8%, 27.9% and 28.6%, respectively. Under the same unloading confining pressure ratio, the greater the initial axial pressure, the greater the porosity, indicating that the increase of initial axial pressure promotes the damage of rock during unloading. The sample enters the plastic deformation stage earlier in the unloading process, and the internal pores of the rock are more

developed and deformed, corresponding to the mechanical test results, the accuracy of the test results is fully proved.

From Fig. 13b, it can be seen that when the unloading confining pressure ratio is 0~75%, the three curves grow slowly and the change of porosity is small, indicating that the pore development of rock is slow and the damage is small at this stage. This is because in the early stage of unloading, the unloading confining pressure is small, and the influence of radial tensile stress is weak. At this stage, the deformation
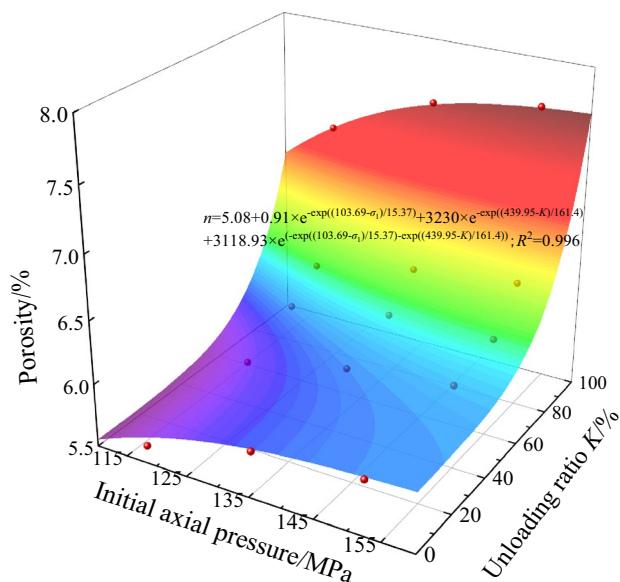

Fig. 14 Relationship between porosity and initial axial pressure and unloading confining pressure ratio

characteristics of rock are mainly elastic deformation. The pores in the sample are still compressed and closed, and the pore development is slow, so the total porosity increases less. In the stage of unloading confining pressure ratio of 75~90%, the increased range of porosity becomes larger, indicating that the development of rock pores is accelerated, the degree of rock damage is intensified, the rock is transformed from elastic deformation to plastic deformation gradually, the internal cracks are expanding, and the rock is gradually deformed macroscopically. In the stage of unloading confining pressure ratio of 90~100%, the sample is damaged and the porosity increases sharply, indicating that the pores in the rock develop rapidly, the fractures enter the stage of unstable expansion, the fractures continue to expand, penetrate until damaged, and the rock damage increases sharply, which shows obvious rock dilatancy characteristics on the macro level.

Considering the influence of initial axial pressure and unloading confining pressure ratio on the porosity change of rock during unloading comprehensively, draw a 3D porosity surface diagram, as shown in Fig. 14, and establish the porosity surface expression based on exponential function fitting. As shown in Eq. (13), the fitting correlation coefficient is as high as 0.996, so it can be considered that the exponential surface expression of porosity is reliable.

$$
\begin{aligned}
n = \ &5.08 + 0.91 \times \exp\left(-e^{(103.69-\sigma_1)/15.37}\right) \\
&+ 3230 \times \exp\left(-e^{(439.95-K)/161.4}\right) \\
&+ 3118.93 \times \exp\left(-e^{(103.69-\sigma_1)/15.37} - e^{(439.95-K)/161.4}\right)
\end{aligned}
\tag{13}
$$

3.3.3 Pore Type

The pore distribution of sandstone after the unloading test is sorted and counted. According to the size of the pores, the pores were divided into micropores (0~0.1 μm), mesopores (0.1~1 μm) and macropores (> 1 μm). According to this classification standard, the proportion of different types of pores in sandstone under different unloading conditions can be sorted out, as shown in Fig. 15. The fitting functions and correlation coefficients for different types of pores are shown in Table 5.

With the increase of unloading confining pressure ratio, the number of micropores continues to increase, and the number of mesopores and macropores first decreases and then increases. In the stage of 0~50% unloading confining pressure ratio, the mesopores and macropores decrease. At this time, the increase in the number of micropores in the sample mainly comes from the reduction of the size of macropores and mesopores under compression, forming new micropores, and the rock is in the stage of elastic compression. In the stage of 50~90% unloading confining pressure
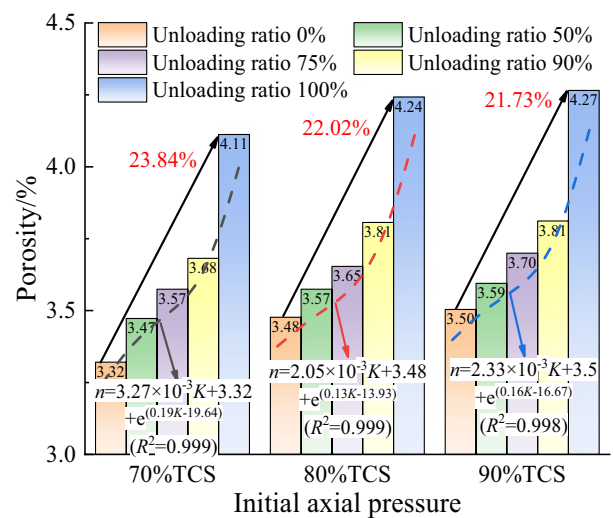
(a) Variation law of 0~0.1 μm micropores
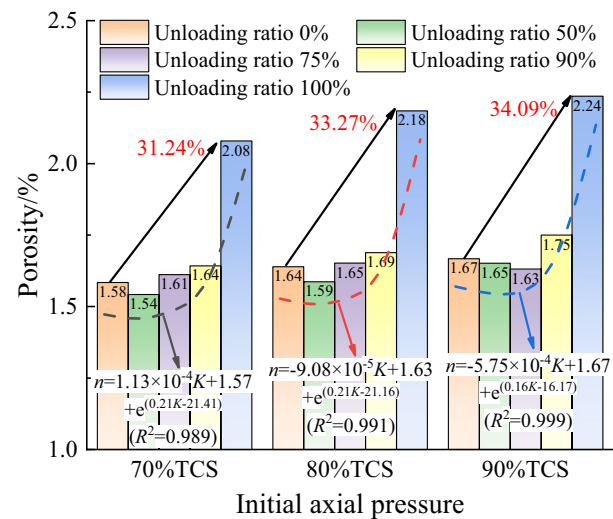
(b) Variation law of 0.1~1 μm mesopores
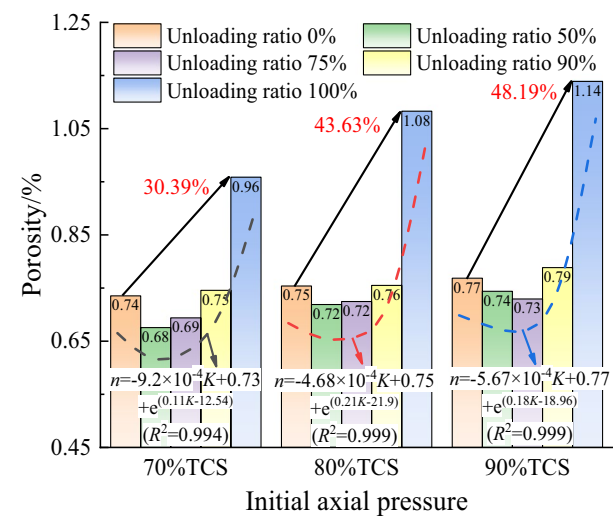
(c) Variation law of >1 μm macropores

Fig. 15 Variation law of different pores

Table 5 Fitting relationship of porosity

Pore type	Initial axial pressure	Porosity n fitting relationship	R^2
Micropores	70%TCS	$n = 3.27 \times 10^{-3} K + 3.318 + \exp(0.189 K\text{-}19.647)$	0.99961
	80%TCS	$n = 2.05 \times 10^{-3} K + 3.476 + \exp(0.133 K\text{-}13.925)$	0.99988
	90%TCS	$n = 2.33 \times 10^{-3} K + 3.498 + \exp(0.16 K\text{-}16.669)$	0.99789
Mesopore	70%TCS	$n = 1.129 \times 10^{-4} K + 1.573 + \exp(0.207 K\text{-}21.412)$	0.98852
	80%TCS	$n = -9.077 \times 10^{-5} K + 1.628 + \exp(0.206 K\text{-}21.159)$	0.99067
	90%TCS	$n = -5.753 \times 10^{-4} K + 1.67 + \exp(0.157 K\text{-}16.171)$	0.99933
Macropore	70%TCS	$n = -9.199 \times 10^{-4} K + 0.732 + \exp(0.114 K\text{-}12.543)$	0.99364
	80%TCS	$n = -4.679 \times 10^{-4} K + 0.751 + \exp(0.209 K\text{-}21.902)$	0.99869
	90%TCS	$n = -5.669 \times 10^{-4} K + 0.769 + \exp(0.181 K\text{-}18.964)$	0.99988

ratio, the number of micropores continues to increase. Under 70% and 80% TCS, the number of mesopores and macropores also changes to increase. Under 90% TCS, the number of mesopores and macropores decreases first and then increases, indicating that the sample continues to be damaged under 70% and 80% TCS. At this stage, part of the increase of micropores still comes from the compaction of mesopores and macropores to form micropores, and part comes from the increase of compressive stress caused by the decrease of radial stress, and new small cracks are generated in the sample gradually, the increase of mesopores and macropores is caused by the continuous development and expansion of micropores and the increase of pore size. Under 90% TCS, the mesopores and macropores decrease slightly, indicating that under the condition of high stress, the mesopores and macropores in the rock are still compacted to form micropores, and the number of micropores formed is more than the number of micropores expanded into mesopores and macropores. With the further increase of unloading confining pressure ratio, the mesopores and macropores increase. At this time, the internal damage of the sample is serious, and the development and expansion of pores intensifies; In the stage of 90~100% unloading confining pressure ratio, the pore diameter of the rock increases greatly. At this time, the penetration degree of pores in the sample intensifies, the cracks expand continuously, the number and size of pores increase sharply, and the internal cracks enter the stage of unstable development, and gradually form a sliding surface until the sample damaged.

Under 70%, 80% and 90% TCS, when the unloading confining pressure ratio increases from 0 to 100%, the increase range of micropores is 23.84%, 22.02% and 21.73%, respectively. The increase range of mesopores is 31.24%, 33.27% and 34.09%, respectively. And the increase range of macropores is 30.39%, 43.63% and 48.19%, respectively. The increase amplitude of micropores decreases with the increase of initial axial pressure, while mesopores and macropores increase with the increase of initial axial pressure. The reason is that at low axial pressure, when the unloading failure of the specimen

occurs, the pore development is not complete, and some micropores do not expand into macropores. The sharp increase of micropores under low axial pressure plays a major role in the damage and failure of rock. Under the condition of high stress, the number of mesopores and macropores accounts for more in the unloading failure of the sample, indicating that the pores with micropore develop and expand more thoroughly, and the rock damage and failure are mainly caused by the continuous development and expansion of micropores into macropores.

4 Discussion

4.1 Rock Damage Evolution Law

Defects lead to a reduction in effective bearing area, which is the main mechanism of material degradation (Zhou et al. 2014b). Accordingly, the concept of continuity φ is introduced:

$$\varphi = \frac{\tilde{A}}{A} \tag{14}$$

where A is the effective bearing area in nondestructive state, and $\tilde{A}$ is the effective bearing area of damage.

Using the concept of representative volume element, it is extended to three-dimensional damage, that is:

$$\varphi = \frac{\tilde{V}}{V} \tag{15}$$

where $\tilde{V}$ is the effective volume in the nondestructive state, and V is the effective volume of damage.

Rabotnov uses the damage degree D, which is a complementary parameter to continuity φ, to characterize the damage and deterioration process of rock(Wang et al. 2022a, b):
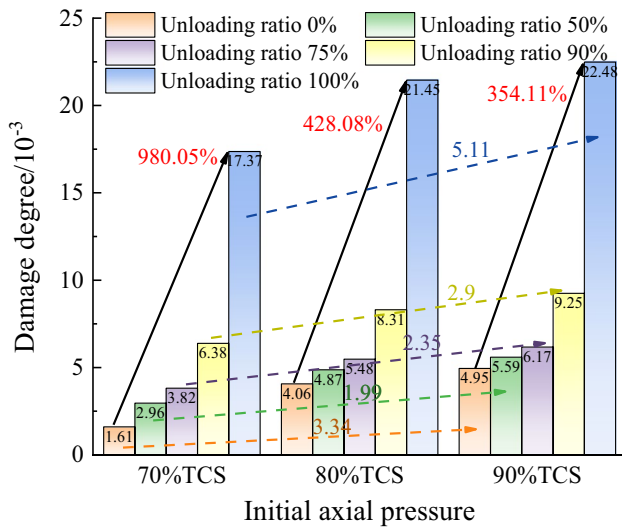
$$D = 1 - \varphi \tag{16}$$

Fig. 16 change trend of damage degree

Fig. 17 Damage evolution process of rock under different conditions

where D is scalar, $D = 0$ is nondestructive state, and $D = 1$ is the theoretical limit damage state, which is complete damage.

The change of pore structure in rock is the result of the generation and development of internal damage in rock, which has an internal inevitable relationship with the damage variables and constitutive relationship of rock materials. Therefore, a rock damage model based on NMR parameters is established by using damage theory. Based on the detection principle of rock pore structure by NMR, it is proposed to characterize the damage degree D of rock by NMR parameter. The damage degree calculation formula of damaged materials can be obtained as follows:

$$D = 1 - \frac{\tilde{V}}{V} = \frac{n - n_0}{1 - n_0} \tag{17}$$

where n_0 is the initial porosity of the rock, 5.47%. n is the porosity of the rock after damage.

Figure 16 shows the change in damage degree of the unloading termination point under different test conditions.

The overall increase in damage was 980.05%, 428.08%, and 354.11% for the increase in the unloading confining pressure ratio from 0 to 100% under 70%, 80%, and 90% TCS, respectively. The larger the initial axial pressure is, the smaller the increase of damage degree at the unloading termination point is, while the damage change of rock during unloading is greater under low axial pressure. At the initial stage of unloading, the damage degree gap caused by initial axial pressure gradually decreases. With the increase of unloading confining pressure ratio, the damage degree of rock increases faster under low axial pressure. In the later stage of unloading, the greater the initial axial pressure, the
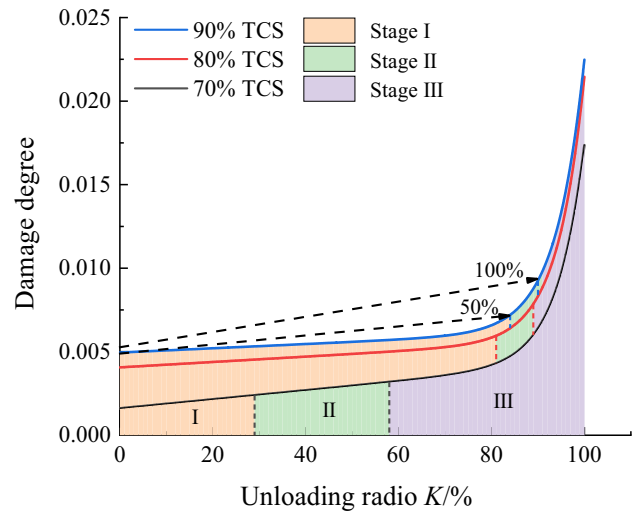
greater the damage increment, and the damage gap under different initial axial pressures gradually increases.

According to the analysis of the test porosity results in Sect. 3.2, there is a high correlation between porosity and the initial axial pressure and unloading confining pressure ratio. Substituting Eqs. (10), (11) and (12) into Eq. (17), (18), (19) and (20) can be used to predict the change of sandstone damage degree with unloading conditions under the test conditions.

$$D_{0.7} = \frac{2.56 \times 10^{-3} K + 0.152 + e^{(0.172K - 16.99)}}{94.53} \tag{18}$$

$$D_{0.8} = \frac{1.52 \times 10^{-3} K + 0.384 + e^{(0.173K - 16.9)}}{94.53} \tag{19}$$

$$D_{0.9} = \frac{1.2 \times 10^{-3} K + 0.468 + e^{(0.164K - 15.97)}}{94.53} \tag{20}$$

Figure 17 shows the change of damage variable d with unloading confining pressure ratio under three axial compression conditions obtained from the above equation. It can be seen that the damage evolution of sandstone can be divided into three stages. The damage degree of stage I does not change much with the increase of unloading confining pressure ratio, and the damage degree increment is less than 50%, and the influence of initial axial pressure on rock damage degree is more significant. The damage degree of stage II begins to increase rapidly, the increase of unloading confining pressure ratio gradually plays a leading role in the rock damage degree, and the damage degree increases by 100%. And the damage degree of stage III increases sharply until rock damage occurs.
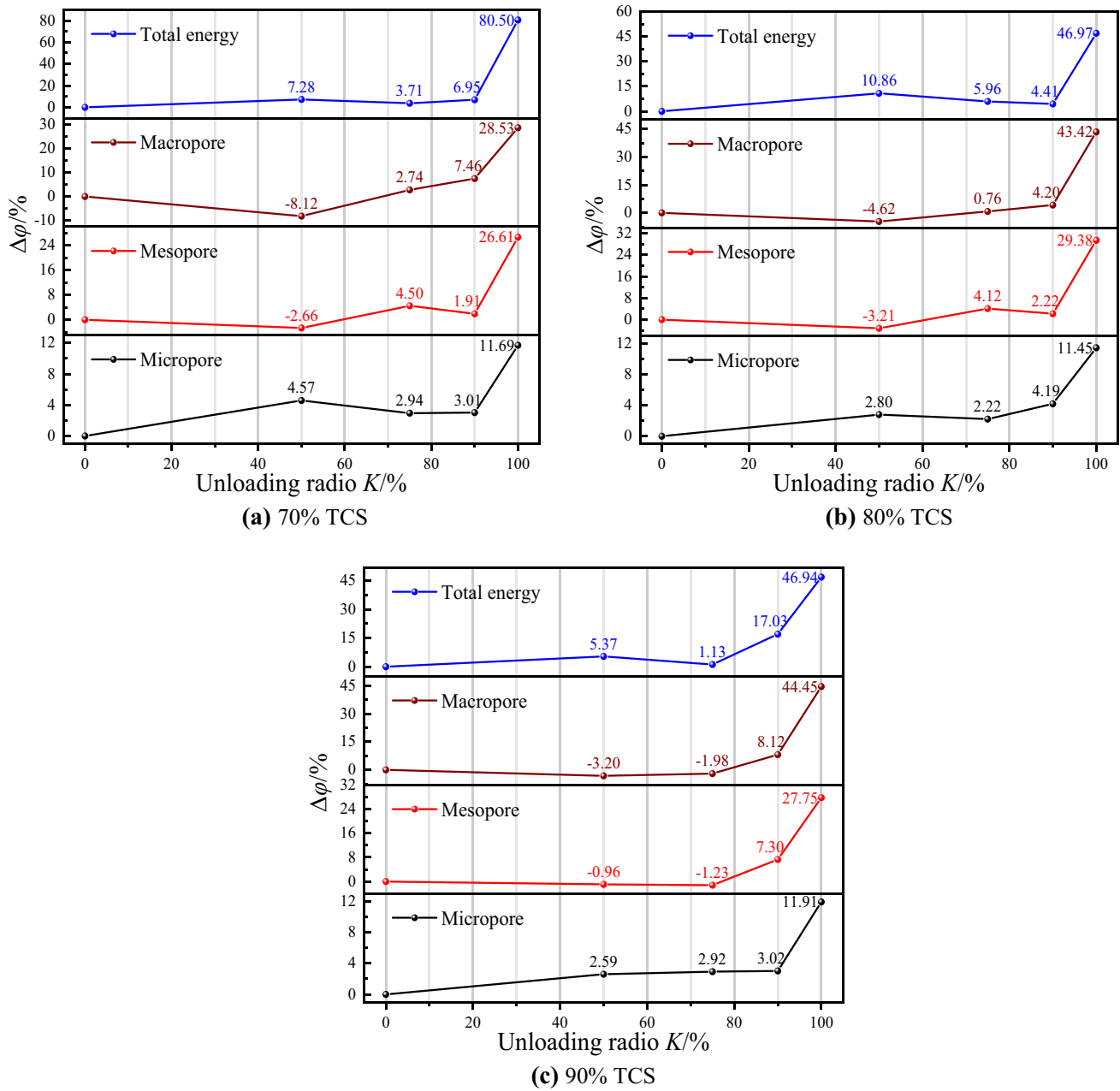
Fig. 18 correspondence between porosity growth rate and total energy growth rate

4.2 Correlation Analysis of Unloading Mechanical Characteristic Parameters of Sandstone

4.2.1 Pore Structure and Energy

The crack propagation and rock deformation in rock are both the results of energy. To study the correlation between the porosity change law and the energy growth trend during the rock test, the relationship between the porosity growth rate ($\Delta\varphi$) and total energy growth rate of three sizes of rock pores under different unloading confining pressure ratios was established. Under 70%, 80% and 90% TCS, with the increase of unloading confining pressure ratio, the porosity growth rate and total energy growth rate curves of three sizes of rock correspond to a–c in Fig. 18, respectively.

From Fig. 18, it can be seen that under 70%, 80% and 90% TCS, with the increase of unloading confining pressure ratio, the growth rate of total energy increases first, then decreases and then increases, while the growth rate of micropores basically increases, then decreases and then increases with the increase of unloading confining pressure

ratio, the change law of total energy and micropores is similar. This phenomenon is caused by the high proportion of micropores in rock, and the structural state of micropores is most easily changed. Therefore, with the change of total energy of rock, the change law of micropores is basically consistent with the change law of total energy. Under 70%, 80% and 90% TCS, when the unloading confining pressure ratio increases from 90 to 100%, the growth rates of total energy of rock is 80.5%, 46.97% and 46.94%, respectively, and the growth rates of macropores are 28.53%, 43.42% and 44.45%, respectively. The increase of macropores during unloading failure depends on the change range of total

energy. The larger the growth rate of macropores, the smaller the growth rate of total energy. This is because the larger the initial axial pressure, the larger the radial strain, which leads to the larger the growth rate of radial strain energy, and the smaller the growth rate of total energy.

With large initial axial pressure, the growth rate of small pores and middle pores is basically unchanged when unloading failure occurs, which fully proves that the increase of axial pressure can promote the development of macropores in rock, and the damage and failure of rock are caused by the significant increase of the number of macropores. By comparing the change rules of growth rate curves in Fig. 18,
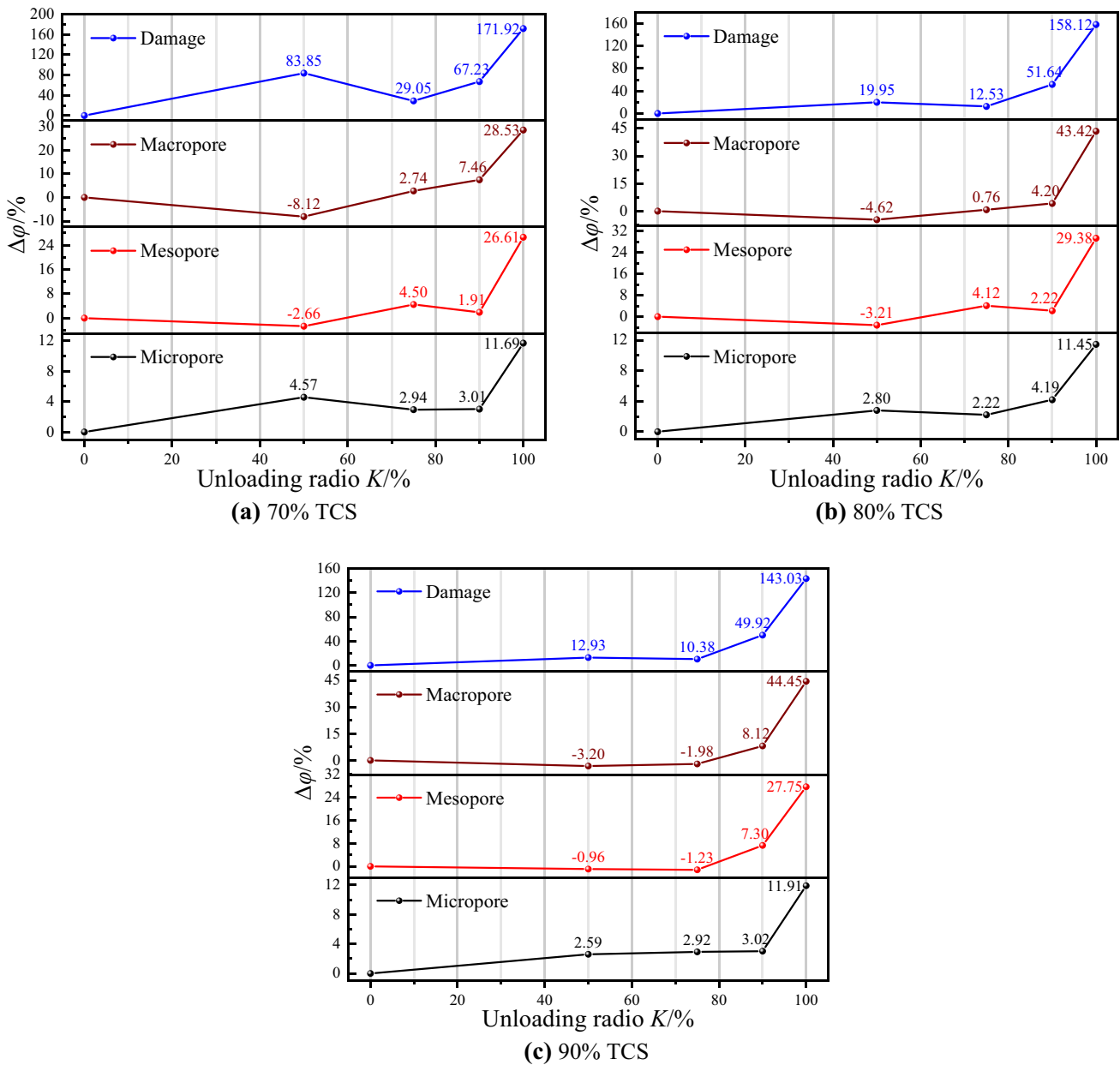

(a) 70% TCS

(b) 80% TCS

(c) 90% TCS

Fig. 19 Correspondence between porosity growth rate and damage growth rate

it is found that the growth rate of macropores fluctuates more than that of mesopores and micropores, and the growth rates of micropores and mesopores are maintained at about 28% and 11%, respectively, when unloading failure occurs, indicating that the development of these two types of pores is restricted to a certain extent. This is because the micropore structure of the rock is unstable during the loading process, which is easy to develop and expand continuously, and then cracks are generated and transformed into lagger pores and macro cracks.

4.2.2 Pore Structure and Damage Degree

The change of pore characteristics is an important factor affecting the degree of rock damage. To study the correlation between the change law of porosity and the growth trend of rock damage degree, the relationship between the growth rate of porosity and the growth rate of damage degree of three sizes of rock pores under different unloading confining pressure ratios was established. Under 70%, 80% and 90% TCS, with the increase of unloading confining pressure ratio, the change trend curves of porosity growth rate and damage growth rate of three sizes of rock correspond to a–c in Fig. 19, respectively.

The change trend of the damage growth rate curve is basically the same as that of the total energy growth rate curve. With the increase of unloading confining pressure ratio, the curves increase first, then decrease and then increase. In the stage of unloading confining pressure ratio 0~50%, the greater the growth rate of micropores, the greater the growth rate of damage degree, which indicates that the damage of rock in the early stage of unloading is mainly caused by the growth of micropores. With the increase of the unloading confining pressure ratio, the growth rate of mesopores and macropores gradually changes from negative to positive and increases continuously. At this stage, the effect of micropores growth on rock damage gradually decreases, and the length of mesopores and macropores plays a major role in rock damage. The change trend of damage degree growth rate under different initial axial pressures is consistent with the total energy when unloading failure occurs. The larger the axial pressure is, the larger the growth rate of macropores is, and the smaller the growth rate of damage degree is.

4.3 Fractal Characteristics of NMR

4.3.1 Fractal Geometric Expression of T_2 Curve

Under different unloading conditions, there are differences in the internal pore characteristics of rocks. Fractal theory is introduced to further characterize the internal structural changes of rocks. Fractal can reflect the space occupation ability of complex bodies and quantitatively describe irregular and non-linear (Song et al. 2021). According to the NMR results, there are mainly three sizes of pores in the rock. Based on fractal theory and NMR characteristics of rocks, the fractal characteristics of pores were obtained. It is assumed that the internal pores of rock have fractal characteristics, and the pore size function distribution of rock pores conforms to $N = \propto r^{-D}$, the number of pores with pore size greater than r follows the power function relationship with r, which can be expressed by the following relationship (Hu et al. 2020; Wan et al. 2010; Zhao et al. 2022):

$$N(> r) = \int_r^{r_{max}} P(r)dr = a \times r^{-d} \tag{21}$$

where r_{max} is the largest reservoir pore radius; $P(r)$ is the pore diameter distribution density function; d is the pore fractal dimension; a is the pore fractal coefficients.

By deriving from both sides of Eq. (21), the expression of $P(r)$ is obtained as follows:

$$P(r) = \frac{dN(> r)}{dr} = -da \times r^{(-d-1)} \tag{22}$$

The cumulative volume of pores with pore size less than r can be expressed as:

$$V(< r) = \int_{r_{min}}^r P(r)Ar^3 dr \tag{23}$$

where A is the constant related to pore shape (when the pore is square, $A = 1$, when the pore is circular, $A = 4\pi/3$), and r_{min} is the minimum pore size.

The following Eq. (24) is obtained by substituting Eq. (22) into Eq. (23):

$$V(< r) = -\frac{daA}{3-d}\left(r^{3-d} - r_{min}^{3-d}\right) \tag{24}$$

When r is the maximum, the total pore volume is:

$$V_s = -\frac{daA}{3-d}\left(r_{max}^{3-d} - r_{min}^{3-d}\right) \tag{25}$$

Since r_{max} is much larger than r_{min}, r_{min} can be ignored. Combining Eq. (24) and Eq. (25), the cumulative pore volume fraction S_v of pore diameter r is:

$$S_v = \frac{V}{V_S} = \frac{r^{3-d} - r_{min}^{3-d}}{r_{max}^{3-d} - r_{min}^{3-d}} = \frac{r^{3-d}}{r_{max}^{3-d}} \tag{26}$$

According to Eq. (22), the pore diameter r is proportional to the transverse relaxation time T_2. Equation (26) can be transformed into:
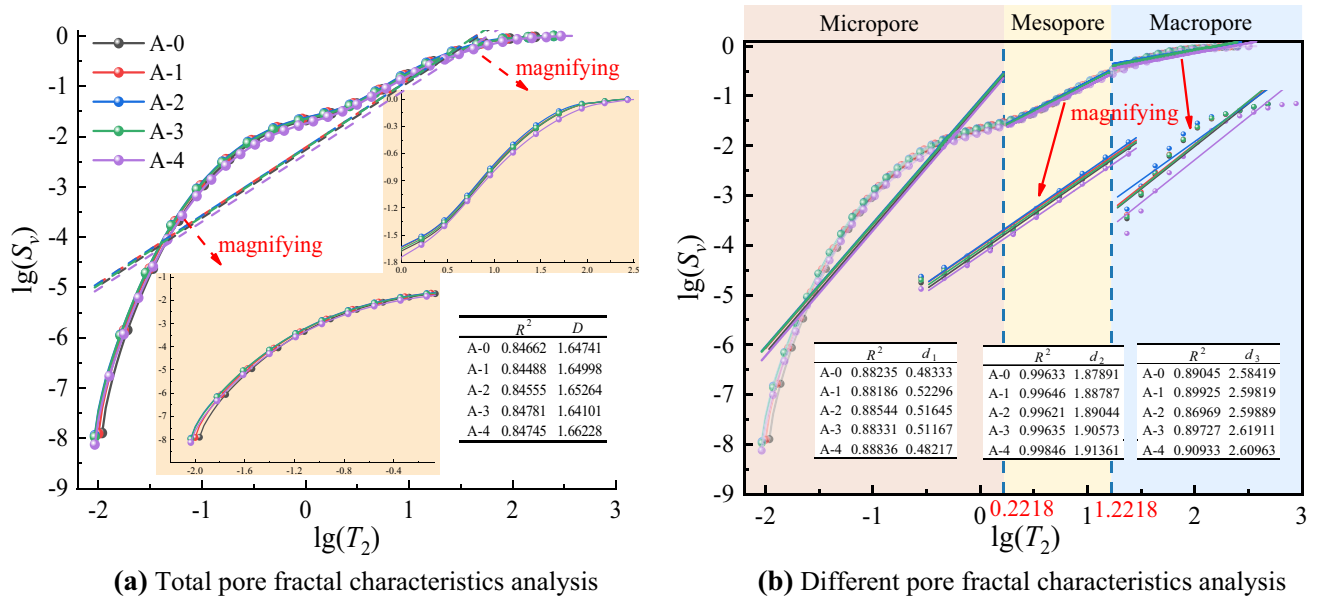
(a) Total pore fractal characteristics analysis

(b) Different pore fractal characteristics analysis

Fig. 20 Analysis of pore fractal characteristics under 70% TCS

(a) Total pore fractal characteristics analysis

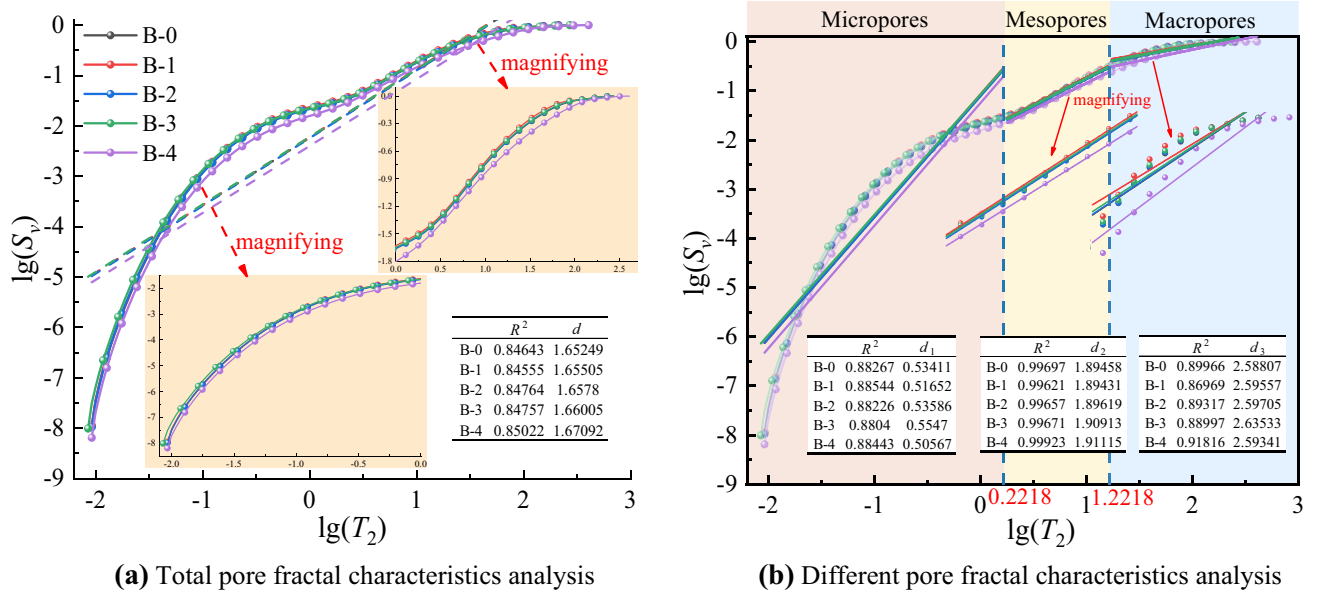**(b)** Different pore fractal characteristics analysis

Fig. 21 Analysis of pore fractal characteristics under 80% TCS

$$S_v = \frac{T_2^{3-d}}{T_{2\max}^{3-d}} \tag{27}$$

where S_v is the percentage between cumulative pore volume with a transverse relaxation time less than T_2 and total pore volume (%), and $T_{2\max}$ is the T_2 value corresponding to the maximum pore radius (ms).

The logarithm of both sides of Eq. (27) can be obtained:

$$\lg(S_v) = (3-d)\lg(T_2) + (d-3)\lg(T_{2\max}) \tag{28}$$

It shows that if the pore structure of rock has fractal characteristics, then $\lg(S_v)$ and $\lg(T_2)$ have linear correlation, and the fractal dimension and maximum relaxation time of the pore structure can be calculated by the least square method. The pore fractal structure characteristics can be obtained according to the correlation coefficient obtained
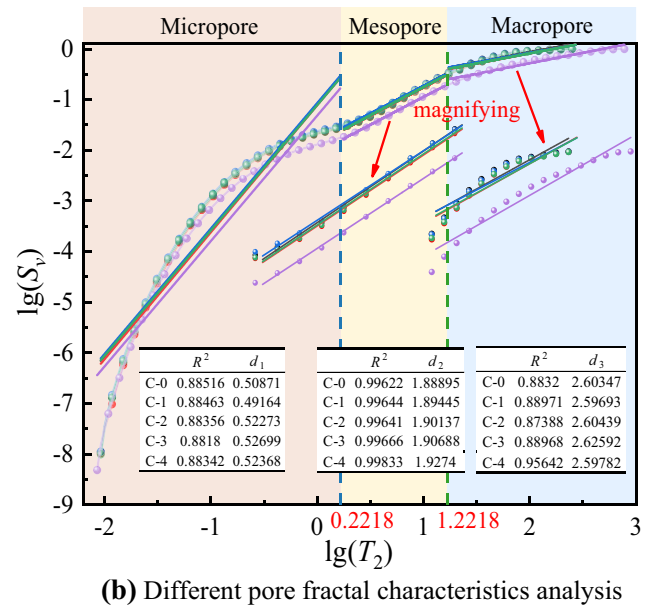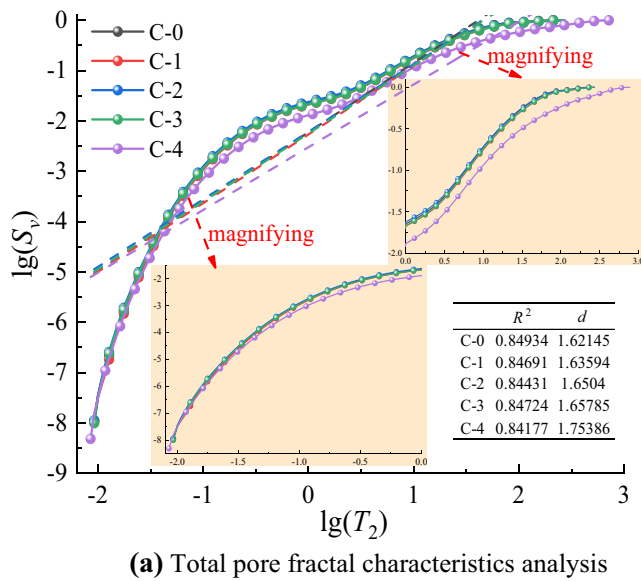
(a) Total pore fractal characteristics analysis

(b) Different pore fractal characteristics analysis

Fig. 22 Analysis of pore fractal characteristics under 90% TCS

by regression analysis. The complexity of pore structure can be judged by the fractal dimension of NMR. The calculation formula of the least square method is:

$$d = 3 - \frac{\sum_{i=1}^{n} x_i y_i - n\overline{xy}}{\sum_{i=1}^{n} x_j^2 - n\overline{x}^2} \tag{29}$$

where x_i and y_j are the data of each point in the curve.

4.3.2 Fractal Dimension Characteristic Analysis

The relationship between the fractal characteristics of each rock pore and the T_2 spectrum curve was established. The fractal dimension of the total pore and the fractal dimension of the three size pores of the rock were calculated as shown in Figs. 20, 21 and 22, respectively. Among them, (a) is the fractal characteristics of the total pore of the rock, and (b) is the fractal characteristics of micropores, mesopores and macropores. The T_2 relaxation time corresponding to 0.1 μm and 1 μm pore size is 1.67 ms and 16.7 ms respectively, and lg (T_2) is 0.2218 and 1.2218, respectively. It can be considered that when lg (T_2) < 0.2218, it is the fractal characteristic curve corresponding to micropores; when 0.2218 < lg (T_2) < 1.2218, it is the fractal characteristic curve corresponding to mesopores; when 1.2218 < lg (T_2), it is the fractal characteristic curve corresponding to macropores. The fitting degree of each linear fitting function of the three sizes of pores is greater than that of the total pore, indicating that the fractal dimension of the total pore is less effective in characterizing the complexity of the rock, and the analysis
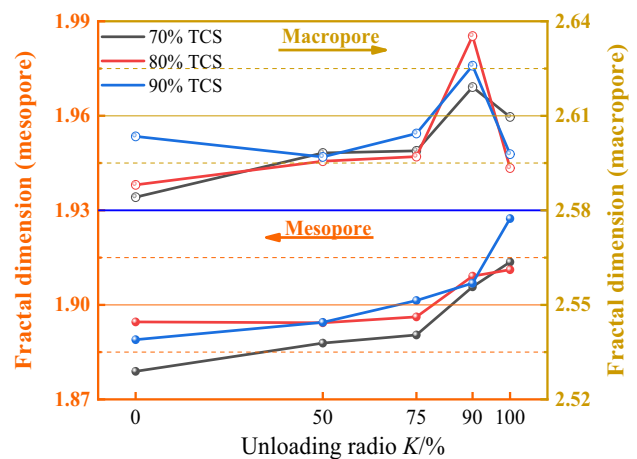

Fig. 23 Variation law of fractal dimensions of mesopores and macropores

of the fractal characteristics of the three sizes of pores is more reliable.

Based on the above calculation results of the fractal dimension, the fractal dimension of macropores is larger than that of mesopores and micropores, which indicates that the structure of macropores is the most complex, and the structure of micropores is less complex. The fractal dimension of the total pores of rock is between micropores and mesopores, which indicates that the overall structural characteristics of rock pores are good. This is due to the large proportion of micropores, which reduces the overall complexity of pores. By comparing the fractal dimensions of three sizes of pores in three groups of A, B and C, the fractal dimension of micropores is weakly affected

by the change of unloading confining pressure ratio and initial axial pressure. This is because the pore size of micropores is small, the pore structure is simple, and the spatial distribution characteristics are single, indicating that with the change of external stress, the spatial structure characteristics of micropores will not produce the complex spatial structure. The fractal dimensions of mesopores and macropores show regularity with the difference in unloading confining pressure ratio and initial axial pressure, as shown in Fig. 23. Under different initial axial pressures, the fractal dimension of the middle pore becomes larger with the increase of the unloading confining pressure ratio. Under different stress conditions, the change of the middle pore is partly from the development and penetration of the micropores, and partly from the compaction of the macropores and the decrease of the pore size, which leads to the complex and changeable structure of the middle pore. The structural complexity of the middle pore is basically consistent with the trend of rock deterioration and damage. With the increase of unloading confining pressure ratio, the fractal dimension of macropores tends to increase first and then decrease. The increase in fractal dimension is related to the damage and deformation of rock internal fractures. However, at the rock failure point, the fractal dimension drops sharply. This is because a large number of fractures intersect and coalesce to expand into macro fracture surfaces when the rock destroyed, and the pore volume and pore diameter increase greatly, while the corresponding pore structure and complexity decrease, resulting in a sharp decrease in the fractal dimension.

5 Conclusions

In this paper, NMR technology and rock unloading mechanical test were combined to study the changes in pore structure and meso damage law of rock under different unloading stress conditions. The following conclusions were obtained:

1. In the process of axial compression loading, the change trend of the axial strain curve of rock is much larger than that of radial strain. In the stage of unloading confining pressure, the change range of radial strain is more obvious. When the unloading failure occurs, the rock shows obvious dilatancy characteristics. The greater the initial axial pressure, the greater the axial strain and the smaller the radial strain when the unloading failure occurs. With the increase of unloading confining pressure ratio, the rock gradually changes from elastic deformation to plastic deformation, the elastic modulus decreases, and the Poisson's ratio and strain increase. The total energy absorbed by the specimen during the test mainly depends on the axial strain energy generated by the axial deformation, and the dissipated energy is mainly used for the development of micro cracks and macro crack growth in the rock sample.

2. There are three peaks in T_2 spectrum curve, indicating that the pore structure in sandstone is complex, mostly micropores. Under different initial axial pressures, with the increase of unloading confining pressure ratio, the area and range of T_2 spectrum curve increase, the pores develop and the pore size increases. The failure of the sample is caused by the rapid increase of the number of pores, the rapid development of pore size and the accelerated expansion of macropores and cracks. With the increase of unloading confining pressure ratio, the number of micropores continues to increase, and the number of mesopores and macropores first decreases and then increases. In the initial stage of unloading, the increase in the number of micropores mainly comes from the reduction of the pore size of macropores and mesopores under compression; In the unloading failure stage, the number and size of pores increase sharply, the internal crack enters the unstable development stage, and gradually forms a sliding surface until the sample is damaged.

3. The porosity increases exponentially with the increase of the unloading confining pressure ratio. When the unloading confining pressure ratio is 0~75%, the porosity growth is small under the three initial axial pressures. At this stage, the development of rock pores is slow and the damage is small; When the unloading confining pressure ratio is 75~90%, the increase range of porosity becomes larger, the development of porosity accelerates, and the degree of rock damage intensifies; When the unloading confining pressure ratio is 90~100%, the sample is damaged, the porosity increases sharply, and the fracture expands and penetrates until rock failure. Under the same unloading confining pressure ratio, the greater the initial axial pressure is, the greater the porosity is, and the initial axial pressure will aggravate the damage of rock during unloading.

4. According to the principle of damage mechanics, the functional relationship between damage degree and unloading confining pressure ratio was established. The damage degree increases with the increase of the unloading confining pressure ratio, which can be divided into three stages. The increase of macropores during unloading failure depends on the change range of total energy. The larger the growth rate of macropores, the smaller the growth rate of total energy. The changing trend of damage degree growth rate under different initial axial pressures is consistent with the total energy when unloading failure occurs. The larger the axial pressure is, the larger the growth rate of macropores is, and the smaller the growth rate of damage degree is. The fractal dimension of micropores is weakly affected by the change in unloading confining pressure ratio and initial axial pressure. The fractal dimensions of mesopores and

macropores show regularity with the difference in unloading confining pressure ratio and initial axial pressure.

Author Contributions JF funding acquisition, writing – review & editing. WC investigation, methodology, writing – original draft. YT writing – review & editing. JW funding acquisition, writing – review & editing. WS funding acquisition, writing – review & editing, supervision.

Data availability The data that support the findings of this study are available on request from the corresponding author.

Declarations

Conflict of Interest The authors declare that the work described has not been published before; that it is not under consideration for publication anywhere else; that its publication has been approved by all coauthors; that there is no conflict of interest regarding the publication of this article.

References

Alam MM, Hjuler ML, Christensen HF, Fabricius IL (2014) Petrophysical and rock-mechanics effects of CO2 injection for enhanced oil recovery: experimental study on chalk from south arne field, North Sea. J Petrol Sci Eng 122:468–487. https://doi.org/10.1016/j.petrol.2014.08.008

Al-Shalabi EW, Sepehrnoori K (2016) A comprehensive review of low salinity/engineered water injections and their applications in sandstone and carbonate rocks. J Petrol Sci Eng 139:137–161. https://doi.org/10.1016/j.petrol.2015.11.027

Barsanescu P (2015) Extension of Mohr–Coulomb theory for ductile materials. Exp Mech 55(7):1389–1393. https://doi.org/10.1007/s11340-015-0026-0

BV (2005) Statistical analysis of the influence of water content on the strength of the miocene limestone. Rock Mech Rock Eng. https://doi.org/10.1007/s00603-004-0034-3

Chen Y, Zuo J, Li Z, Dou R (2020) Experimental investigation on the crack propagation behaviors of sandstone under different loading and unloading conditions. Int J Rock Mech Min 130:104310. https://doi.org/10.1016/j.ijrmms.2020.104310

Chu ZF, Wu ZJ, Liu QS, Weng L, Wang ZY, Zhou Y (2021) Evaluating the microstructure evolution behaviors of saturated sandstone using NMR testing under uniaxial short-term and creep compression. Rock Mech Rock Eng 54(9):4905–4927. https://doi.org/10.1007/s00603-021-02538-4

Connolly PRJ, Yan W, Zhang D et al (2019) Simulation and experimental measurements of internal magnetic field gradients and NMR transverse relaxation times (T2) in sandstone rocks. J Petrol Sci Eng 175:985–997. https://doi.org/10.1016/j.petrol.2019.01.036

Dai B, Zhao G, Konietzky H, Wasantha PLP (2018) Experimental investigation on damage evolution behaviour of a granitic rock under loading and unloading. J Cent South Univ 25(5):1213–1225. https://doi.org/10.1007/s11771-018-3819-3

Ding Q, Ju F, Mao X, Ma D, Yu B, Song S (2016) Experimental investigation of the mechanical behavior in unloading conditions of sandstone after high-temperature treatment. Rock Mech Rock Eng 49(7):2641–2653. https://doi.org/10.1007/s00603-016-0944-x

Diyuan L, Zhi S, Quanqi Z, Kang P (2019) Triaxial loading and unloading tests on dry and saturated sandstone specimens. Appl Sci. https://doi.org/10.3390/app9081689

Duan K, Ji Y, Wu W, Kwok CY (2019) Unloading-induced failure of brittle rock and implications for excavation-induced strain burst. Tunn Undergr Sp Tech 84:495–506. https://doi.org/10.1016/j.tust.2018.11.012

Feng Q, Jiang B (2015) Analytical solution for stress and deformation of the mining floor based on integral transform. Int J Min Sci Technol 25(4):581–586. https://doi.org/10.1016/j.ijmst.2015.05.010

Fu J, Cao S, Song W, Tan Y (2017a) Creep analysis and delay time of instability of ultrahigh pillar considering initial imperfections. J China Univ Min Technol 46(02):279–284. https://doi.org/10.13247/j.cnki.jcumt.000645

Fu J, Song W, Tan Y (2017b) Criterion of local energy release rate of gob instability in deep mines considering unloading stress path. Int J Min Sci Technol 27(6):1011–1017. https://doi.org/10.1016/j.ijmst.2017.06.008

Fu J, Song W, Tan Y (2018) Study of stability and evolution indexes of gobs under unloading effect in the deep mines. Geomech Eng 14(5):439–451. https://doi.org/10.12989/gae.2018.14.5.439

Fu J, Wang J, Song W (2020) Damage constitutive model and strength criterion of cemented paste backfill based on layered effect considerations. J Market Res 9(3):6073–6084. https://doi.org/10.1016/j.jmrt.2020.04.011

Gao F, Wang Q, Deng H, Zhang J, Tian W, Ke B (2017) Coupled effects of chemical environments and freeze-thaw cycles on damage characteristics of red sandstone. B Eng Geol Environ 76(4):1481–1490. https://doi.org/10.1007/s10064-016-0908-0

Hou G, Liang J, Jing H, Tan J, Zhang Y, Yang X (2020a) Experimental study on deformation and acoustic emission characteristics of arch roadway under different unloading rates. Adv Civ Eng. https://doi.org/10.1155/2020/8818242

Hou G, Liang J, Jing H et al (2020b) Influence of deviatoric stress on the deformation and damage evolution of surrounding rock under unloading conditions. Shock Vib. https://doi.org/10.1155/2020/3158209

Hou ZY, Hao CB, Xiao FK, Liu G (2021) Research on energy conversion and damage features of unloading instability of sandstone under high stress. Adv Civ Eng. https://doi.org/10.1155/2021/6655968

Hu Z, Zhou K, Li J, Gao F, Wang M (2014) Meso-damage evolution of unloading rock mass based on nuclear magnetic resonance technology. Chin J Eng 36(12):1567–1574. https://doi.org/10.13374/j.issn1001-053x.2014.12.001

Hu JH, Ren QF, Yang DJ et al (2020) Cross -scale characteristics of backfill material using NMR and fractal theory. Trans Nonferr Metal Soc 30(5):1347–1363. https://doi.org/10.1016/S1003-6326(20)65301-8

Huang RQ, Huang D (2014) Evolution of rock cracks under unloading condition. Rock Mech Rock Eng 47(2):453–466. https://doi.org/10.1007/s00603-013-0429-0

Huang D, Li Y (2014) Conversion of strain energy in triaxial unloading tests on marble. Int J Rock Mech Min 66:160–168. https://doi.org/10.1016/j.ijrmms.2013.12.001

Kang P, Jing Z, Quanle Z, Xiao S (2020) Deformation characteristics of granites at different unloading rates after high-temperature treatment. Environ Earth Sci 79(13):343. https://doi.org/10.1007/s12665-020-09088-y

Li D, Zhao F, Zheng M (2014) Fractal characteristics of cracks and fragments generated in unloading rockburst tests. Int J Min Sci

Technol 24(6):819–823. https://doi.org/10.1016/j.ijmst.2014.10.014

Li X, Chen Z, Weng L, Li C (2019) Unloading responses of pre-flawed rock specimens under different unloading rates. T Nonferr Metal Soc 29(7):1516–1526. https://doi.org/10.1016/S1003-6326(19)65059-4

Li H, Zhong Z, Eshiet KI, Sheng Y, Liu X, Yang D (2020) Experimental investigation of the permeability and mechanical behaviours of chemically corroded limestone under different unloading conditions. Rock Mech Rock Eng 53(4):1587–1603. https://doi.org/10.1007/s00603-019-01961-y

Lin Y, Zhou K, Li J, Ke B, Gao R (2020) Weakening laws of mechanical properties of sandstone under the effect of chemical corrosion. Rock Mech Rock Eng 53(4):1857–1877. https://doi.org/10.1007/s00603-019-01998-z

Lyu C, Ning Z, Cole DR, Wang Q, Chen M (2020) Experimental investigation on T2 cutoffs of tight sandstones: comparisons between outcrop and reservoir cores. J Petrol Sci Eng 191:107184. https://doi.org/10.1016/j.petrol.2020.107184

Martini F, Borsacchi S, Geppi M, Tonelli M, Ridi F, Calucci L (2018) Monitoring the hydration of MgO-based cement and its mixtures with portland cement by 1H NMR relaxometry. Micropor Mesopor Mat 269:26–30. https://doi.org/10.1016/j.micromeso.2017.05.031

Meng Q, Zhang M, Han L, Pu H, Nie T (2016) Effects of acoustic emission and energy evolution of rock specimens under the uniaxial cyclic loading and unloading compression. Rock Mech Rock Eng 49(10):3873–3886. https://doi.org/10.1007/s00603-016-1077-y

Nasharuddin R, Luo G, Robinson N, Fourie A, Johns ML, Fridjonsson EO (2021) Understanding the microstructural evolution of hypersaline cemented paste backfill with low-field NMR relaxation. Cement Concrete Res 147:106516. https://doi.org/10.1016/j.cemconres.2021.106516

Olatinsu OB, Olorode DO, Clennell B, Esteban L, Josh M (2017) Lithotype characterizations by nuclear magnetic resonance (NMR): a case study on limestone and associated rocks from the Eastern Dahomey Basin, Nigeria. J Afr Earth Sci 129:701–712. https://doi.org/10.1016/j.jafrearsci.2017.02.005

Shen Y, Wang Y, Wei X, Jia H, Yan R (2020) Investigation on meso-debonding process of the sandstone-concrete interface induced by freeze-thaw cycles using NMR technology. Constr Build Mater 252:118962. https://doi.org/10.1016/j.conbuildmat.2020.118962

Song Y, Yang H, Tan H, Ren J, Guo X (2021) Study on damage evolution characteristics of sandstone with different saturations in freeze-thaw environment. Chin J Rock Mech Eng 40(08):1513–1524. https://doi.org/10.13722/j.cnki.jrme.2021.0089

Teng T, Peng G (2020) Experimental and theoretical study on the compression characteristics of dry/water-saturated sandstone under different deformation rates. Arab J Geosci. https://doi.org/10.1007/s12517-020-05552-y

Wan CZ, Ting TW, Guo SJ, Da CZ (2010) The study on fractal damage of rock under hydraulic fracturing basing on conversation of energy. Appl Mech Mater. https://doi.org/10.4028/www.scientific.net/amm.29-32.1363

Wang J, Fu J, Song W, Zhang Y, Wang Y (2020) Mechanical behavior, acoustic emission properties and damage evolution of cemented paste backfill considering structural feature. Constr Build Mater 261:119958. https://doi.org/10.1016/j.conbuildmat.2020.119958

Wang J, Zhang C, Fu J, Song W, Zhang Y (2021a) Effect of water saturation on mechanical characteristics and damage behavior of cemented paste backfill. J Market Res 15:6624–6639. https://doi.org/10.1016/j.jmrt.2021.11.078

Wang J, Fu J, Song W, Zhang Y (2021b) Mechanical properties, damage evolution, and constitutive model of rock-encased backfill under uniaxial compression. Constr Build Mater 285:122898. https://doi.org/10.1016/j.conbuildmat.2021.122898

Wang J, Fu J, Song W, Zhang Y, Wu S (2021c) Acoustic emission characteristics and damage evolution process of layered cemented tailings backfill under uniaxial compression. Constr Build Mater 295:123663. https://doi.org/10.1016/j.conbuildmat.2021.123663

Wang J, Fu J, Song W, Zhang Y (2022a) Effect of rice husk ash (RHA) dosage on pore structural and mechanical properties of cemented paste backfill. J Market Res 17:840–851. https://doi.org/10.1016/j.jmrt.2022.01.044

Wang J, Zhang Q, Song Z, Liu X, Wang X, Zhang Y (2022b) Microstructural variations and damage evolvement of salt rock under cyclic loading. Int J Rock Mech Min 152:105078. https://doi.org/10.1016/j.ijrmms.2022.105078

Wen T, Tang H, Ma J, Liu Y (2019) Energy analysis of the deformation and failure process of sandstone and damage constitutive model. Ksce J Civ Eng 23(2):513–524. https://doi.org/10.1007/s12205-018-0789-9

Xie H, Li L, Peng R, Ju Y (2009) Energy analysis and criteria for structural failure of rocks. J Rock Mech Geotech Eng 1(1):11–20. https://doi.org/10.3724/SP.J.1235.2009.00011

Xue J, Du X, Ma Q, Zhan K (2021) Experimental study on law of limit storage energy of rock under different confining pressures. Arab J Geosci 14(1):62. https://doi.org/10.1007/s12517-020-06398-0

Zhang HQ, Tannant DD, Jing HW, Nunoo S, Niu SJ, Wang SY (2015) Evolution of cohesion and friction angle during microfracture accumulation in rock. Nat Hazards 77(1):497–510. https://doi.org/10.1007/s11069-015-1592-2

Zhang D, Yang Y, Chu Y, Zhang X, Xue Y (2018) Influence of loading and unloading velocity of confining pressure on strength and permeability characteristics of crystalline sandstone. Results Phys 9:1363–1370. https://doi.org/10.1016/j.rinp.2018.04.043

Zhang C, Fu J, Song W, Du C, Fu H (2021a) High-volume ultrafine fly ash-cement slurry mechanical properties and strength development model establishment. Constr Build Mater 277:122350. https://doi.org/10.1016/j.conbuildmat.2021.122350

Zhang L, Cong Y, Meng F, Wang Z, Zhang P, Gao S (2021b) Energy evolution analysis and failure criteria for rock under different stress paths. Acta Geotech 16(2):569–580. https://doi.org/10.1007/s11440-020-01028-1

Zhao XG, Wang J, Cai M et al (2014) Influence of unloading rate on the strainburst characteristics of beishan granite under true-triaxial unloading conditions. Rock Mech Rock Eng 47(2):467–483. https://doi.org/10.1007/s00603-013-0443-2

Zhao F, Hu J, Yang Y, Xiao H, Ma F (2022) Cross-scale study on lime modified phosphogypsum cemented backfill by fractal theory. Minerals-Basel. https://doi.org/10.3390/MIN12040403

Zhou K, Hu Z, Li J, Gao F, Wang M (2014a) Study of marble damage evolution laws under unloading conditions based on nuclear magnetic resonance technique. Chin J Rock Mech Eng 33(S2):3523–3530. https://doi.org/10.13722/j.cnki.jrme.2014.s2.016

Zhou K, Hu Z, Gao F, Wang M, Yang Z (2014b) Study of marble damage laws under triaxial compression condition based on nuclear magnetic resonance technique. Rock Soil Mech 35(11):3117–3122. https://doi.org/10.16285/j.rsm.2014.11.008

Zhou K, Su S, Hu Z, Li J, Yang Z (2015) Experimental research into nuclear magnetic resonance in marble with different initial damages under unloading conditions. Rock Soil Mech 36(08):2144–2150. https://doi.org/10.16285/j.rsm.2015.08.003

Zhou K, Liu T, Hu Z (2018a) Exploration of damage evolution in marble due to lateral unloading using nuclear magnetic resonance. Eng Geol 244:75–85. https://doi.org/10.1016/j.enggeo.2018.08.001

Zhou C, Ren F, Zeng Q, Xiao L, Wang W (2018b) Pore-size resolved water vapor adsorption kinetics of white cement mortars as viewed from proton NMR relaxation. Cement Concrete Res 105:31–43. https://doi.org/10.1016/j.cemconres.2017.12.002

Zhou X, Pan X, Cheng H (2021a) The nonlinear creep behaviors of sandstone under the different confining pressures based on NMR technology. Rock Mech Rock Eng 54(9):4889–4904. https://doi.org/10.1007/s00603-021-02557-1

Zhou TB, Qin YP, Cheng J, Zhang XY, Ma QF (2021b) Study on damage evolution model of sandstone under triaxial loading and postpeak unloading considering nonlinear behaviors. Geofluids. https://doi.org/10.1155/2021/2395789

Zilong Z, Xin C, Wenzhuo C, Xibing L, Cheng X (2016) Influence of water content on mechanical properties of rock in both saturation and drying processes. Rock Mech Rock Eng. https://doi.org/10.1007/s00603-016-0987-z